First measurement of neutron capture multiplicity in neutrino-oxygen neutral-current quasi-elastic-like interactions using an accelerator neutrino beam

K. Abe,[61] S. Abe,[61] R. Akutsu,[16] H. Alarakia-Charles,[34] Y.I. Alj Hakim,[55] S. Alonso Monsalve,[9] L. Anthony,[21]
S. Aoki,[32] K.A. Apte,[21] T. Arai,[60] T. Arihara,[64] S. Arimoto,[33] Y. Ashida,[70] E.T. Atkin,[21] N. Babu,[38]
V. Baranov,[39] G.J. Barker,[71] G. Barr,[47] D. Barrow,[47] P. Bates,[37] L. Bathe-Peters,[47] M. Batkiewicz-Kwasniak,[15]
N. Baudis,[47] V. Berardi,[22] L. Berns,[70] S. Bhattacharjee,[38] A. Blanchet,[11] A. Blondel,[58, 12] P.M.M. Boistier,[5]
S. Bolognesi,[5] S. Bordoni,[12] S.B. Boyd,[71] C. Bronner,[73] A. Bubak,[56] M. Buizza Avanzini,[36] J.A. Caballero,[54]
F. Cadoux,[12] N.F. Calabria,[22] S. Cao,[20] S. Cap,[12] D. Carabadjac,[36, *] S.L. Cartwright,[55] M.P. Casado,[18, †]
M.G. Catanesi,[22] J. Chakrani,[35] A. Chalumeau,[58] D. Cherdack,[17] A. Chvirova,[26] J. Coleman,[37] G. Collazuol,[24]
F. Cormier,[66] A.A.L. Craplet,[21] A. Cudd,[6] D. D'ago,[24] C. Dalmazzone,[58] T. Daret,[5] P. Dasgupta,[8] C. Davis,[48]
Yu.I. Davydov,[39] P. de Perio,[29] G. De Rosa,[23] T. Dealtry,[34] C. Densham,[44] A. Dergacheva,[26] R. Dharmapal
Banerjee,[72] F. Di Lodovico,[31] G. Diaz Lopez,[58] S. Dolan,[11] D. Douqa,[12] T.A. Doyle,[43] O. Drapier,[36] K.E. Duffy,[47]
J. Dumarchez,[58] P. Dunne,[21] K. Dygnarowicz,[69] A. Eguchi,[60] J. Elias,[50] S. Emery-Schrenk,[5] G. Erofeev,[26]
A. Ershova,[36] G. Eurin,[5] D. Fedorova,[26] S. Fedotov,[26] M. Feltre,[24] L. Feng,[33] D. Ferlewicz,[60] A.J. Finch,[34]
M.D. Fitton,[44] C. Forza,[24] M. Friend,[16, ‡] Y. Fujii,[16, ‡] Y. Fukuda,[41] Y. Furui,[64] J. García-Marcos,[14] A.C. Germer,[48]
L. Giannessi,[12] C. Giganti,[58] M. Girgus,[68] V. Glagolev,[39] M. Gonin,[28] R. González Jiménez,[54] J. González Rosa,[54]
E.A.G. Goodman,[13] K. Gorshanov,[26] P. Govindaraj,[68] M. Grassi,[24] M. Guigue,[58] F.Y. Guo,[43] D.R. Hadley,[71]
S. Han,[33, 62] D.A. Harris,[74] R.J. Harris,[34, 44] T. Hasegawa,[16, ‡] C.M. Hasnip,[11] S. Hassani,[5] N.C. Hastings,[16]
Y. Hayato,[61, 29] I. Heitkamp,[70] D. Henaff,[5] Y. Hino,[16] J. Holeczek,[56] A. Holin,[44] T. Holvey,[47] N.T. Hong Van,[27]
T. Honjo,[46] M.C.F. Hooft,[14] K. Hosokawa,[61] J. Hu,[33] A.K. Ichikawa,[70] K. Ieki,[61] M. Ikeda,[61] T. Ishida,[16, ‡]
M. Ishitsuka,[65] H. Ito,[32] S. Ito,[73] A. Izmaylov,[26] N. Jachowicz,[14] S.J. Jenkins,[37] C. Jesús-Valls,[11] M. Jia,[43]
J.J. Jiang,[43] J.Y. Ji,[43] T.P. Jones,[34] P. Jonsson,[21] S. Joshi,[5] M. Kabirnezhad,[21] A.C. Kaboth,[51] H. Kakuno,[64]
J. Kameda,[61] S. Karpova,[12] V.S. Kasturi,[12] Y. Kataoka,[61] T. Katori,[31] A. Kawabata,[30] Y. Kawamura,[46]
M. Kawaue,[33] E. Kearns,[2, §] M. Khabibullin,[26] A. Khotjantsev,[26] T. Kikawa,[33] S. King,[31] V. Kiseeva,[39] J. Kisiel,[56]
A. Klustová,[21] L. Kneale,[55] H. Kobayashi,[60] L. Koch,[19] S. Kodama,[60] M. Kolupanova,[26] A. Konaka,[66]
L.L. Kormos,[34] Y. Koshio,[45, §] K. Kowalik,[42] Y. Kudenko,[26, ¶] Y. Kudo,[73] A. Kumar Jha,[14] R. Kurjata,[69]
V. Kurochka,[26] T. Kutter,[38] L. Labarga,[1] M. Lachat,[50] K. Lachner,[9] J. Lagoda,[42] S.M. Lakshmi,[56] M. Lamers
James,[71] A. Langella,[23] D.H. Langridge,[51] J.-F. Laporte,[5] D. Last,[50] N. Latham,[31] M. Laveder,[24] L. Lavitola,[23]
M. Lawe,[34] D. Leon Silverio,[59] S. Levorato,[24] S.V. Lewis,[31] B. Li,[9] C. Lin,[21] R.P. Litchfield,[13] S.L. Liu,[43] W. Li,[47]
A. Longhin,[24] A. Lopez Moreno,[31] L. Ludovici,[25] X. Lu,[71] T. Lux,[18] L.N. Machado,[13] L. Magaletti,[22] K. Mahn,[40]
K.K. Mahtani,[43] S. Manly,[50] A.D. Marino,[6] D.G.R. Martin,[21] D.A. Martinez Caicedo,[59] L. Martinez,[18]
M. Martini,[58, **] T. Matsubara,[16] R. Matsumoto,[63] V. Matveev,[26] C. Mauger,[48] K. Mavrokoridis,[37] N. McCauley,[37]
K.S. McFarland,[50] C. McGrew,[43] J. McKean,[21] A. Mefodiev,[26] G.D. Megias,[54] L. Mellet,[40] C. Metelko,[37]
M. Mezzetto,[24] S. Miki,[61] V. Mikola,[13] E.W. Miller,[18] A. Minamino,[73] O. Mineev,[26] S. Mine,[61, 4] J. Mirabito,[2]
M. Miura,[61, §] S. Moriyama,[61, §] S. Moriyama,[73] P. Morrison,[13] Th.A. Mueller,[36] D. Munford,[17] A. Muñoz,[36, 28]
L. Munteanu,[11] Y. Nagai,[8] T. Nakadaira,[16, ‡] K. Nakagiri,[60] M. Nakahata,[61, 29] Y. Nakajima,[60] K.D. Nakamura,[70]
A. Nakano,[70] Y. Nakano,[67] S. Nakayama,[61, 29] T. Nakaya,[33, 29] K. Nakayoshi,[16, ‡] C.E.R. Naseby,[21] D.T. Nguyen,[10]
V.Q. Nguyen,[36] K. Niewczas,[14] S. Nishimori,[16] Y. Nishimura,[30] Y. Noguchi,[61] T. Nosek,[42] F. Nova,[44] J.C. Nugent,[21]
H.M. O'Keeffe,[34] L. O'Sullivan,[19] R. Okazaki,[30] W. Okinaga,[60] K. Okumura,[62, 29] T. Okusawa,[46] N. Onda,[33]
N. Ospina,[22] L. Osu,[36] N. Otani,[33] Y. Oyama,[16, ‡] V. Paolone,[49] J. Pasternak,[21] D. Payne,[37] M. Pfaff,[21]
L. Pickering,[44] B. Popov,[58, ††] A.J. Portocarrero Yrey,[16] M. Posiadala-Zezula,[68] Y.S. Prabhu,[68] H. Prasad,[72]
F. Pupilli,[24] B. Quilain,[28, 36] P.T. Quyen,[20, ‡‡] E. Radicioni,[22] B. Radics,[74] M.A. Ramirez,[48] R. Ramsden,[31]
P.N. Ratoff,[34] M. Reh,[6] G. Reina,[19] C. Riccio,[43] D.W. Riley,[13] E. Rondio,[42] S. Roth,[52] N. Roy,[74] A. Rubbia,[9]
L. Russo,[58] A. Rychter,[69] W. Saenz,[58] K. Sakashita,[16, ‡] S. Samani,[12] F. Sánchez,[12] E.M. Sandford,[37] Y. Sato,[65]
T. Schefke,[38] K. Scholberg,[7, §] M. Scott,[21] Y. Seiya,[46, §§] T. Sekiguchi,[16, ‡] H. Sekiya,[61, 29, §] T. Sekiya,[64]
D. Seppala,[40] D. Sgalaberna,[9] A. Shaikhiev,[26] M. Shiozawa,[61, 29] Y. Shiraishi,[45] A. Shvartsman,[26] N. Skrobova,[26]
K. Skwarczynski,[51] D. Smyczek,[52] M. Smy,[4] J.T. Sobczyk,[72] H. Sobel,[4, 29] F.J.P. Soler,[13] A.J. Speers,[34] R. Spina,[22]
A. Srivastava,[19] P. Stowell,[55] Y. Stroke,[26] I.A. Suslov,[39] A. Suzuki,[32] S.Y. Suzuki,[16, ‡] M. Tada,[16, ‡] S. Tairafune,[70]
A. Takeda,[61] Y. Takeuchi,[32, 29] K. Takeya,[45] H.K. Tanaka,[61, §] H. Tanigawa,[16] V.V. Tereshchenko,[39] N. Thamm,[52]
C. Touramanis,[37] N. Tran,[33] T. Tsukamoto,[16, ‡] M. Tzanov,[38] Y. Uchida,[21] M. Vagins,[29, 4] M. Varghese,[18]
I. Vasilyev,[39] G. Vasseur,[5] E. Villa,[11, 12] U. Virginet,[58] T. Vladisavljevic,[44] T. Wachala,[15] S.-i. Wada,[32]
D. Wakabayashi,[70] H.T. Wallace,[55] J.G. Walsh,[40] D. Wark,[44, 47] M.O. Wascko,[47, 44] A. Weber,[19] R. Wendell,[33]

M.J. Wilking,[53] C. Wilkinson,[35] J.R. Wilson,[31] K. Wood,[35] C. Wret,[21] J. Xia,[57] K. Yamamoto,[46, §§]
T. Yamamoto,[46] C. Yanagisawa,[43, ¶¶] Y. Yang,[47] T. Yano,[61] N. Yershov,[26] U. Yevarouskaya,[43] M. Yokoyama,[60, §]
Y. Yoshimoto,[60] N. Yoshimura,[33] R. Zaki,[74] A. Zalewska,[15] J. Zalipska,[42] G. Zarnecki,[15] J. Zhang,[66, 3]
X.Y. Zhao,[9] H. Zheng,[43] H. Zhong,[32] T. Zhu,[21] M. Ziembicki,[69] E.D. Zimmerman,[6] M. Zito,[58] and S. Zsoldos[31]
(The T2K Collaboration)

[1] *University Autonoma Madrid, Department of Theoretical Physics, 28049 Madrid, Spain*
[2] *Boston University, Department of Physics, Boston, Massachusetts, U.S.A.*
[3] *University of British Columbia, Department of Physics and Astronomy, Vancouver, British Columbia, Canada*
[4] *University of California, Irvine, Department of Physics and Astronomy, Irvine, California, U.S.A.*
[5] *IRFU, CEA, Université Paris-Saclay, F-91191 Gif-sur-Yvette, France*
[6] *University of Colorado at Boulder, Department of Physics, Boulder, Colorado, U.S.A.*
[7] *Duke University, Department of Physics, Durham, North Carolina, U.S.A.*
[8] *Eötvös Loránd University, Department of Atomic Physics, Budapest, Hungary*
[9] *ETH Zurich, Institute for Particle Physics and Astrophysics, Zurich, Switzerland*
[10] *VNU University of Science, Vietnam National University, Hanoi, Vietnam*
[11] *CERN European Organization for Nuclear Research, CH-1211 Genéve 23, Switzerland*
[12] *University of Geneva, Section de Physique, DPNC, Geneva, Switzerland*
[13] *University of Glasgow, School of Physics and Astronomy, Glasgow, United Kingdom*
[14] *Ghent University, Department of Physics and Astronomy, Proeftuinstraat 86, B-9000 Gent, Belgium*
[15] *H. Niewodniczanski Institute of Nuclear Physics PAN, Cracow, Poland*
[16] *High Energy Accelerator Research Organization (KEK), Tsukuba, Ibaraki, Japan*
[17] *University of Houston, Department of Physics, Houston, Texas, U.S.A.*
[18] *Institut de Fisica d'Altes Energies (IFAE) - The Barcelona Institute*
of Science and Technology, Campus UAB, Bellaterra (Barcelona) Spain
[19] *Institut für Physik, Johannes Gutenberg-Universität Mainz, Staudingerweg 7, 55128 Mainz, Germany*
[20] *Institute For Interdisciplinary Research in Science and Education (IFIRSE), ICISE, Quy Nhon, Vietnam*
[21] *Imperial College London, Department of Physics, London, United Kingdom*
[22] *INFN Sezione di Bari and Università e Politecnico di Bari, Dipartimento Interuniversitario di Fisica, Bari, Italy*
[23] *INFN Sezione di Napoli and Università di Napoli, Dipartimento di Fisica, Napoli, Italy*
[24] *INFN Sezione di Padova and Università di Padova, Dipartimento di Fisica, Padova, Italy*
[25] *INFN Sezione di Roma and Università di Roma "La Sapienza", Roma, Italy*
[26] *Institute for Nuclear Research of the Russian Academy of Sciences, Moscow, Russia*
[27] *International Centre of Physics, Institute of Physics (IOP), Vietnam Academy*
of Science and Technology (VAST), 10 Dao Tan, Ba Dinh, Hanoi, Vietnam
[28] *ILANCE, CNRS – University of Tokyo International Research Laboratory, Kashiwa, Chiba 277-8582, Japan*
[29] *Kavli Institute for the Physics and Mathematics of the Universe (WPI), The University*
of Tokyo Institutes for Advanced Study, University of Tokyo, Kashiwa, Chiba, Japan
[30] *Keio University, Department of Physics, Kanagawa, Japan*
[31] *King's College London, Department of Physics, Strand, London WC2R 2LS, United Kingdom*
[32] *Kobe University, Kobe, Japan*
[33] *Kyoto University, Department of Physics, Kyoto, Japan*
[34] *Lancaster University, Physics Department, Lancaster, United Kingdom*
[35] *Lawrence Berkeley National Laboratory, Berkeley, California, U.S.A.*
[36] *Ecole Polytechnique, IN2P3-CNRS, Laboratoire Leprince-Ringuet, Palaiseau, France*
[37] *University of Liverpool, Department of Physics, Liverpool, United Kingdom*
[38] *Louisiana State University, Department of Physics and Astronomy, Baton Rouge, Louisiana, U.S.A.*
[39] *Joint Institute for Nuclear Research, Dubna, Moscow Region, Russia*
[40] *Michigan State University, Department of Physics and Astronomy, East Lansing, Michigan, U.S.A.*
[41] *Miyagi University of Education, Department of Physics, Sendai, Japan*
[42] *National Centre for Nuclear Research, Warsaw, Poland*
[43] *State University of New York at Stony Brook, Department of Physics and Astronomy, Stony Brook, New York, U.S.A.*
[44] *STFC, Rutherford Appleton Laboratory, Harwell Oxford, and Daresbury Laboratory, Warrington, United Kingdom*
[45] *Okayama University, Department of Physics, Okayama, Japan*
[46] *Osaka Metropolitan University, Department of Physics, Osaka, Japan*
[47] *Oxford University, Department of Physics, Oxford, United Kingdom*
[48] *University of Pennsylvania, Department of Physics and Astronomy, Philadelphia, Pennsylvania, U.S.A.*
[49] *University of Pittsburgh, Department of Physics and Astronomy, Pittsburgh, Pennsylvania, U.S.A.*
[50] *University of Rochester, Department of Physics and Astronomy, Rochester, New York, U.S.A.*
[51] *Royal Holloway University of London, Department of Physics, Egham, Surrey, United Kingdom*
[52] *RWTH Aachen University, III. Physikalisches Institut, Aachen, Germany*
[53] *School of Physics and Astronomy, University of Minnesota, Minneapolis, Minnesota, U.S.A.*
[54] *Departamento de Física Atómica, Molecular y Nuclear, Universidad de Sevilla, 41080 Sevilla, Spain*

[55] *University of Sheffield, School of Mathematical and Physical Sciences, Sheffield, United Kingdom*
[56] *University of Silesia, Institute of Physics, Katowice, Poland*
[57] *SLAC National Accelerator Laboratory, Stanford University, Menlo Park, California, U.S.A.*
[58] *Sorbonne Université, CNRS/IN2P3, Laboratoire de Physique Nucléaire et de Hautes Energies (LPNHE), Paris, France*
[59] *South Dakota School of Mines and Technology, 501 East Saint Joseph Street, Rapid City, SD 57701, United States*
[60] *University of Tokyo, Department of Physics, Tokyo, Japan*
[61] *University of Tokyo, Institute for Cosmic Ray Research, Kamioka Observatory, Kamioka, Japan*
[62] *University of Tokyo, Institute for Cosmic Ray Research, Research Center for Cosmic Neutrinos, Kashiwa, Japan*
[63] *Institute of Science Tokyo, Department of Physics, Tokyo*
[64] *Tokyo Metropolitan University, Department of Physics, Tokyo, Japan*
[65] *Tokyo University of Science, Faculty of Science and Technology, Department of Physics, Noda, Chiba, Japan*
[66] *TRIUMF, Vancouver, British Columbia, Canada*
[67] *University of Toyama, Department of Physics, Toyama, Japan*
[68] *University of Warsaw, Faculty of Physics, Warsaw, Poland*
[69] *Warsaw University of Technology, Institute of Radioelectronics and Multimedia Technology, Warsaw, Poland*
[70] *Tohoku University, Faculty of Science, Department of Physics, Miyagi, Japan*
[71] *University of Warwick, Department of Physics, Coventry, United Kingdom*
[72] *Wroclaw University, Faculty of Physics and Astronomy, Wroclaw, Poland*
[73] *Yokohama National University, Department of Physics, Yokohama, Japan*
[74] *York University, Department of Physics and Astronomy, Toronto, Ontario, Canada*

(Dated: July 14, 2025)

We report the first measurement of neutron capture multiplicity in neutrino-oxygen neutral-current quasi-elastic-like interactions at the gadolinium-loaded Super-Kamiokande detector using the T2K neutrino beam, which has a peak energy of about 0.6 GeV. A total of 30 neutral-current quasi-elastic-like event candidates were selected from T2K data corresponding to an exposure of 1.76×10^{20} protons on target. The γ ray signals resulting from neutron captures were identified using a neural network. The flux-averaged mean neutron capture multiplicity was measured to be 1.37 ± 0.33 (stat.) $^{+0.17}_{-0.27}$ (syst.), which is compatible within 2.3 sigma than predictions obtained using our nominal simulation. We discuss potential sources of systematic uncertainty in the prediction and demonstrate that a significant portion of this discrepancy arises from the modeling of hadron-nucleus interactions in the detector medium.

I. INTRODUCTION

Precise measurements of neutral-current quasi-elastic (NCQE) interactions on oxygen, the dominant neutral-current process at neutrino energies of approximately 0.1 - 1 GeV, are crucial for searches involving rare processes in water Cherenkov detectors. For example, searches for the diffuse supernova neutrino background (DSNB) [1, 2] face significant background contributions from NCQE interactions of atmospheric neutrinos, which are affected by large uncertainties. The NCQE interactions between $\nu(\bar{\nu})$ and ^{16}O can be expressed [3] as follows:

$$\begin{aligned} \nu(\bar{\nu}) + {}^{16}\mathrm{O} &\rightarrow \nu(\bar{\nu}) + {}^{15}\mathrm{O} + \gamma + n \\ \nu(\bar{\nu}) + {}^{16}\mathrm{O} &\rightarrow \nu(\bar{\nu}) + {}^{15}\mathrm{N} + \gamma + p. \end{aligned} \qquad (1)$$

The recoil nucleon is subject to final state interactions as it propagates through the initial target nucleus, which can alter the particle's kinematics, generate additional recoil particles, or induce nuclear de-excitation processes that emit γ rays. Additionally, nucleons escaping the nucleus may undergo further nucleon-nucleus interactions as they traverse the detector medium, collectively labelled as secondary interactions. Following such interactions, the excited nucleus promptly de-excites to its ground state, emitting secondary γ rays in addition to the initial (primary) γ, as well as neutrons or other particles. These primary and secondary γ rays can be used to identify NCQE interactions and were used in a previous T2K publication [4] to measure the flux-averaged NCQE interaction cross section. Recoil hadrons were not measured in that study, though neutrons can be identified via de-excitation γ rays emitted when they capture on detector nuclei.

Precise knowledge of the neutron capture multiplicity is critical for estimation of background to the inverse beta decay signal of DSNB events, which are expected

---

[*] also at Université Paris-Saclay

[†] also at Departament de Fisica de la Universitat Autonoma de Barcelona, Barcelona, Spain.

[‡] also at J-PARC, Tokai, Japan

[§] affiliated member at Kavli IPMU (WPI), the University of Tokyo, Japan

[¶] also at Moscow Institute of Physics and Technology (MIPT), Moscow region, Russia and National Research Nuclear University "MEPhI", Moscow, Russia

[**] also at IPSA-DRII, France

[††] also at JINR, Dubna, Russia

[‡‡] also at the Graduate University of Science and Technology, Vietnam Academy of Science and Technology

[§§] also at Nambu Yoichiro Institute of Theoretical and Experimental Physics (NITEP)

[¶¶] also at BMCC/CUNY, Science Department, New York, New York, U.S.A.

to have exactly one neutron, from atmospheric NCQE events, which are often accompanied by multiple neutrons. While previous measurements have been made with atmospheric neutrinos by SK [5, 6], they suffer large uncertainties from the flux model and from lower signal purity due to contamination of non-NCQE interactions as well as accidental-coincidence backgrounds. Those studies also indicate that secondary interactions have a large impact on the number of neutrons populating the final state in Monte Carlo (MC) simulations. The T2K neutrino beam, with an energy range similar to that of atmospheric neutrino backgrounds to DSNB searches, offers a nearly ideal means of overcoming these limitations. Not only does the beam timing allow for precise selection of signal events and for background rejection, but the tightly constrained flux at T2K allows for smaller uncertainties on both the measurements of NCQE interaction cross section and the neutron capture multiplicity.

This paper reports the first neutron capture multiplicity measurement of neutral-current quasi-elastic-like (NCQE-like) interactions with the T2K neutrino beam. In the following, the term “NCQE-like” is used inclusively to denote the topology listed in Eq. (1) as well as neutral-current two-particle two-hole (NC 2p2h) interactions. NC 2p2h can eject an extra np, nn, or pp pair, adding recoil nucleons that mimic the NCQE signal [4].

This article is organized as follows. The experiment is described in Sec. II while Sec. III describes the event simulation. Details of the event reconstruction and selection methods, including the neutron detection method, are given in Sec. IV. Finally, the results and discussion are given in Secs. V and VI, before concluding in Sec. VII.

II. THE T2K EXPERIMENT

The T2K experiment [7] is a long-baseline accelerator neutrino experiment using the J-PARC neutrino beam as well as a suite of near and far detectors for its measurements. Its primary physics program consists of precision measurements of the neutrino oscillation parameters and detailed studies of neutrino interactions at both its near and far detectors.

While T2K has operated with different configurations since the start of operations in 2009, this study focuses on data taken between March 9, 2021, and April 27, 2021, known as Run 11 and corresponding to 1.76×10^{20} protons on target (POT), for which the following beam settings apply. The neutrino beam production begins with protons grouped into eight bunches per spill with each bunch separated by approximately 581 ns. The J-PARC Main Ring synchrotron accelerates these bunches to 30 GeV/c and directs them to a graphite target in the neutrino beamline with a 2.48-second repetition rate [8]. Hadrons emerging from the proton-target interaction, such as pions and kaons, are focused along the proton beam direction and charge-selected by three magnetic horns [9] operated at ±250 kA. Pions and kaons decay within a dedicated 96 m decay volume located downstream of the magnetic horns, producing neutrinos along the beamline direction. During Run 11 the horns were operated at +250 kA, which focuses positively charged hadrons and produces a predominantly muon neutrino beam from their decays. At the end of the decay volume, a beam dump, a muon monitor [10], and WAGASCI-BabyMIND [11] are positioned to indirectly monitor the neutrino beam’s direction, width, and yield. The near detector complex, consisting of the INGRID [12] and ND280 [13, 14] detectors, is located 280 meters downstream of the graphite target. INGRID is placed on the neutrino beam axis and is responsible for monitoring the direction and intensity of the neutrino beam. ND280, on the other hand, is located 2.5° off-axis and measures the neutrino energy spectrum and the neutrino flavor composition of the beam before neutrino oscillation effects become significant.

The Super-Kamiokande (SK) detector [15, 16] serves as T2K’s far detector, used to study neutrino oscillations and, in this analysis, the neutrino neutral-current interactions. SK is located 295 kilometers downstream and sits 2.5° off-axis with respect to the proton direction. It is a cylindrical 50 kiloton water Cherenkov detector consisting of an inner detector (ID) and an outer detector (OD) that is located 1 km underground. The ID, which measures 33.8 meters in diameter and 36.2 meters in height, is equipped with 11,129 inward-facing photomultiplier tubes (PMT), each 20 inches in diameter. Functioning primarily as a veto, the OD is a 2-meter-thick cylindrical shell surrounding the ID, which is viewed by 1,885 8-inch outward-facing PMTs. The OD is separated from the ID by an uninstrumented region 55 cm in width.

Beam timing information is synchronized between J-PARC and SK using a GNSS system. At SK, a dedicated event trigger is issued corresponding to the beam arrival time, and it initiates recording of all PMT hit charges and times in a time period of 500 μs before and after the trigger. In 2020, 13 tons of $Gd_2(SO_4)_3 \cdot 8H_2O$ were dissolved into SK, leading to a Gd concentration of 0.011%(becomes 0.01% later), for the purpose of enhancing SK’s neutron detection capability. For this reason, the Run 11 data set has significantly enhanced neutron detection capabilities compared to the earlier pure water data taken at T2K. Further details on this upgrade to SK are provided in Ref. [16].

III. EVENT SIMULATION

This study employs a multi-stage simulation in the T2K experiment, simulating the neutrino flux, neutrino-nucleus interactions, and the detector response.

A. Neutrino Flux

The neutrino beam flux calculation uses simulations incorporating FLUKA [17] and GEANT3 [18]. These packages simulate hadronic interactions, particle transport, and particle decay within the neutrino beamline. The production cross sections for pions and kaons are renormalized based on data from the NA61/SHINE experiment, which utilizes a replica of the T2K targets [19] as well as thin targets [20–22]. Using NA61/SHINE 2009 replica-target data, the new flux tuning [23] lowers the peak-region uncertainty from 9–12% to 5–8% for the primary ν_μ fluxes, while the wrong-sign components ($\bar{\nu}_\mu$) remain limited by off-target interactions to 6–8%.

The flux peaks at approximately 0.6 GeV with a width of a few hundred MeV and consists predominantly of ν_μ ($\sim$92.4%) and $\bar{\nu}_\mu$($\sim$6.4%).

Fig. 1 illustrates the predicted neutrino flux at SK in the absence of neutrino oscillations for the data set used in this analysis.

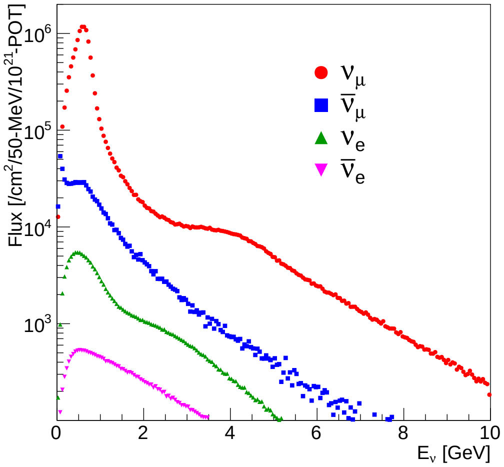

FIG. 1. The predicted neutrino flux for T2K Run 11 at SK without neutrino oscillations.

B. Neutrino Interaction

The NEUT MC code(version 5.6.3) [27, 28] is used to simulate neutrino-nucleon interactions as well as subsequent intranuclear reactions (henceforth referred to as "final state interactions" or FSI) between outgoing hadrons and the ^{16}O nuclear medium. These interactions can result in altered hadron kinematics, particle absorption, or the production of new hadrons, making the hadrons observed outside the nucleus different from those initially produced. NEUT uses the Bertini intranuclear cascade model [29] to propagate nucleons in a semi-classical manner through the nucleus, calculating interaction probabilities at each propagation step based on the Woods-Saxon nuclear density profile [30]. For NCQE and charged-current quasi-elastic (CCQE) interactions, the nucleon momentum distribution is based on the spectral function by Benhar et al. [31, 32]. This study employs the NEUT 5.6.3 default settings, using a dipole form factor with the axial-vector mass set to $M_A^{\mathrm{QE}} = 1.21$ GeV/c^2, the strange axial coupling constant (g_A^s) set to 0.0, and the Fermi momentum for oxygen is set to 209 MeV/c. NEUT incorporates BBBA05 vector form factors [33]. The Valencia model by Nieves et al. [34] is used to simulate charged-current two-particle two-hole (2p2h) interactions, while NC 2p2h interactions are not included. Single pion production is simulated using the Rein and Sehgal model [35–37], with the axial-vector mass set to $M_A^{\mathrm{RES}} = 0.95$ GeV/c^2. Deep inelastic scattering is simulated based on the GRV98 parton distribution [38], with additional corrections from Bodek and Yang [39]. The neutrino interaction parameters used in NEUT for this study are summarized in Table I.

Nuclear de-excitation is also simulated by NEUT. After an initial neutrino-nucleus interaction, the excited state of the nucleus in Eq. (1) is determined based on probabilities outlined in Ref. [3], with possible states including $(p_{1/2})^{-1}$, $(p_{3/2})^{-1}$, $(s_{1/2})^{-1}$ and others. The respective production probabilities are 0.158, 0.3515, 0.1055, and 0.385. The decay products of each state and their branching ratios are summarized in Ref. [26], based on γ ray branching ratio measurements reported in Refs.[40–42]. The *others* category, for which γ ray emission measurements are lacking, is treated identically to the $(s_{1/2})^{-1}$ simulations.

C. Detector Simulation

Interactions between particles and water to produce and propagate Cherenkov photons are modelled by the SK detector simulation as well as the subsequent response of hit PMTs.

Two simulation packages are employed in our study: SKDETSIM [7], which is based on GEANT3 (GEANT3.2.1) [43], and SKG4 [44], which is built using GEANT4 (GEANT4.10.5p01) [25]. This study's primary MC is based on SKDETSIM due to its consistent use throughout the history of both SK and T2K. SKG4 is additionally adopted to make use of the extensive array of hadron-nucleus interaction models (termed "secondary interaction" or SI models below). SKDETSIM and SKG4 are individually calibrated to accurately model the transport of Cherenkov photons and the PMT response. This includes the calibration of the optical scattering processes, photon absorption, the asymmetry of the water quality between the top and bottom regions of the detector, the reflection of light by detector materials, as well as the charge and timing response of the PMTs. Additional details are provided in Ref. [45].

Since neutrons produced through NCQE interactions typically have kinetic energies around $\mathcal{O}(100)$ MeV at

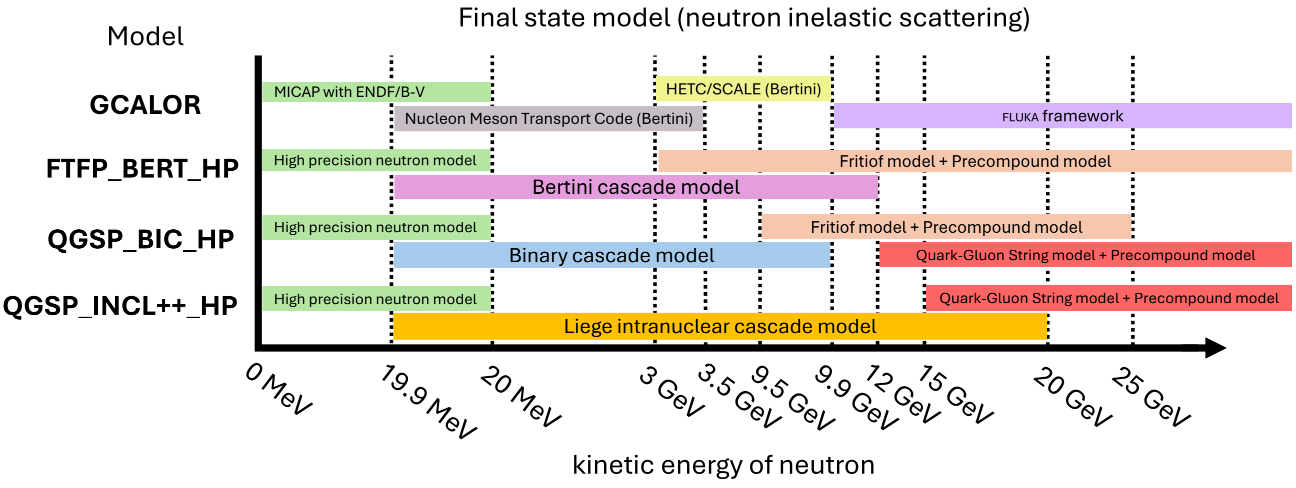

FIG. 2. Illustration of various "physics lists" used for neutron inelastic scattering in SKDETSIM and SKG4. The horizontal axis indicates the kinetic energy of the incoming neutron. A physics list in GEANT4 defines which interaction models and cross sections are used over different energy ranges. In this study, SKDETSIM (based on GEANT3) employs GCALOR [24], while SKG4 (based on GEANT4) can choose from multiple physics lists [25, 26]. Examples include FTFP_BERT_HP (Fritiof Parton & Precompound + Bertini Cascade + High Precision neutron model), QGSP_BIC_HP (Quark-Gluon String & Precompound + BInary Cascade + High Precision neutron model), and INCL++_HP (Liège INtranuclear Cascade + High Precision neutron model).

TABLE I. Model configuration in NEUT 5.6.3.

Channel	Model	Parameter	Value or model
NCQE	Ankowski et al.[3]	M_A^{QE}	1.21 GeV
		g_A^s	0.0
		Fermi momentum	209 MeV/c
		VFF	BBBA05[33]
		Nuclear model	Spectral Function[31, 32]
CCQE	Ankowski et al.[3]	Nuclear model	Spectral Function[31, 32]
CC 2p2h	Nieves et al.[34]		
CC and NC RES	Rein and Sehgal [35]	FF	Dipole form
		M_A^{RES}	0.95 GeV
CC and NC DIS	GRV98 PDF[38]	with modification by Bodek and Yang[39]	
CC and NC COH	Berger-Sehgal[36]		
FSI	NEUT cascade	Nucleon cross section	Bertini et al.[29]

T2K, neutron-nucleus interactions can significantly affect the observed result. The choice of SI model can therefore create notable differences in the total number of predicted γ rays and neutrons. SKDETSIM is the primary choice in this study, which adopts the GCALOR [24] model. However, for neutron energies below 20 MeV MICAP [46] is employed, which models neutrons, nuclei, and neutron capture by hydrogen based on experimental cross section data from the ENDF/B-V library [47]. For nucleon propagation above 20 MeV, GCALOR invokes NMTC [48], which handles nucleons up to 3.5 GeV and charged pions up to 2.5 GeV. At energies just exceeding these thresholds, the HETC/SCALE approach [49], which is based on the Bertini cascade, is used. Finally, FLUKA [17] is applied when energies exceed 10 GeV.

SKG4 is employed in order to evaluate the impact of different SI models using the "physics list" mechanism provided in GEANT4 [25]. Three physics lists are chosen in this study: `FTFP_BERT_HP` (BERT), `QGSP_INCL++_HP` (INCL++), and `QGSP_BIC_HP` (BIC). The Bertini cascade model (BERT) [50] has been widely used in GEANT3 and GEANT4 simulations. The Liège Intranuclear cascade model (INCL++) [51] and the Binary Cascade model (BIC) use the binary cascade approach [52]. The primary distinction among BERT, INCL++, and BIC lies in their criteria for terminating the intranuclear cascade process and their selection of de-excitation model. While the BERT model is known for its relatively simple and highly parameterized pre-equilibrium and nuclear de-excitation models [50], INCL++ and BIC adopt a more detailed nuclear de-excitation model, `G4PreCompoundModel` [53], which offers better precision. These differences lead to varied neutron capture multiplicity predictions as is demonstrated below. Fig. 2 provides an overview of the SI interaction models used in this study.

The SK upgrade [16] enhances neutron detection efficiency by taking advantage of Gd's large neutron capture cross section and the emission of γ rays totaling approximately 8 MeV in energy during de-excitation. The natural abundance of ^{157}Gd and ^{155}Gd are 15.65% and 14.80% [54] and at a neutron energy of approximately 0.0253 eV their capture cross sections are 254,000 and 60,900 barns, respectively [55]. These can be compared with hydrogen's cross section of 0.33 barns [55]. Consequently, with a Gd concentration around 0.011%, approximately 52% of neutrons will be captured on Gd nuclei. This study adopts the ANNRI-Gd model [56] from GEANT4 to model γ ray emission from Gd nuclear de-excitation following neutron capture.

IV. EVENT RECONSTRUCTION AND SELECTION

NCQE-like events are characterized by a delayed pair of triggers in the detector, one occurring promptly after the expected arrival time of the neutrino beam, followed by one or more delayed triggers within the same beam spill window, with spills arriving every 2.48 seconds. Triggers are issued to record all the PMT charge and timing information in a time period of 500 μs before and after the beam arrival time in this analysis. Fig. 3 illustrates the target topology. The prompt event consists of one or more γ rays produced by the de-excitation of nuclear remnant produced by the ν-^{16}O NCQE-like interaction. Additional γ rays may be produced within a time window up to a few tens of nanoseconds by the secondary interactions of hadrons. However, this timescale is too fast to be resolved by the SK detector. On the other hand, the delayed signal is observed on much longer timescales, arising from γ rays emitted when neutrons produced in the initial interaction or subsequent secondary interactions are captured by nuclei in the detector, predominantly gadolinium or hydrogen. In this analysis, a 0.01% concentration of Gd corresponds to a characteristic capture time of 115±1 μs [16]. We note that, while the trigger defining the primary event is required to be consistent with the beam timing, there is no such restriction on the delayed signal.

A. Prompt Event Search

The BONSAI reconstruction algorithm [57], which is optimized for events with visible energies below approximately 50 MeV, is used to analyze the PMT hit pattern and timing of events within a 1.3 μs time window surrounding a trigger. Its vertex and direction reconstruction are based on a maximum likelihood method, assuming a single particle generated all detected light from a single vertex. A Cherenkov angle (θ_C) for the event is obtained by calculating the cone angles between the event vertex and all hit PMT triplets within a 15 ns time trigger timing window, then defining θ_C as the peak of the resulting cone angle distribution. The reconstructed energy for the event (E_rec) is based on a relationship between energy and the calibrated PMT hits. Further details on the algorithm, its performance, and calibration are provided in Ref. [57].

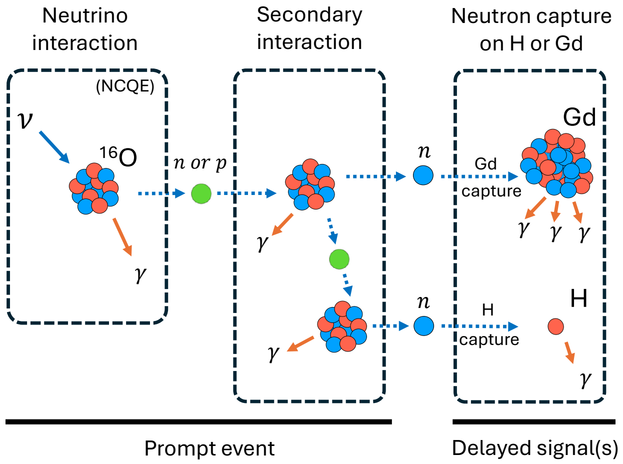

FIG. 3. Schematic of the NCQE interaction. The γ emission from the primary neutrino interaction and the following final state interaction, including secondary nuclear interactions, marks the "prompt" event, while the produced neutrons are captured by hydrogen or gadolinium, accompanied by the delayed γ emission, representing the "delayed" signal.

This study examines five event categories: neutrino NCQE interactions (ν-NCQE), antineutrino NCQE interactions ($\bar{\nu}$-NCQE), other NC interactions (NC-other), CC interactions, and beam-unrelated backgrounds. The NC-other and CC categories incorporate both neutrino and antineutrino contributions. The NC-other category includes NC 1π production, deep inelastic scattering, elastic scattering, and rare channels like eta- and K-meson production. NEUT is used to simulate the first four interactions. Beam-unrelated backgrounds, on the other hand, are estimated from the data set collected in the period from 500 to 5 μs before the beam arrives in SK. This period is termed the Off-Beam time window. Similarly, the On-Beam window is defined as the period from the beam spill arrival (0 ns) to 500 μs afterwards. The event selection criteria below have been optimized to identify the prompt event from ν-NCQE events and $\bar{\nu}$-NCQE events, while minimizing backgrounds from the other event categories.

The complete list of prompt event selection criteria are as follows:

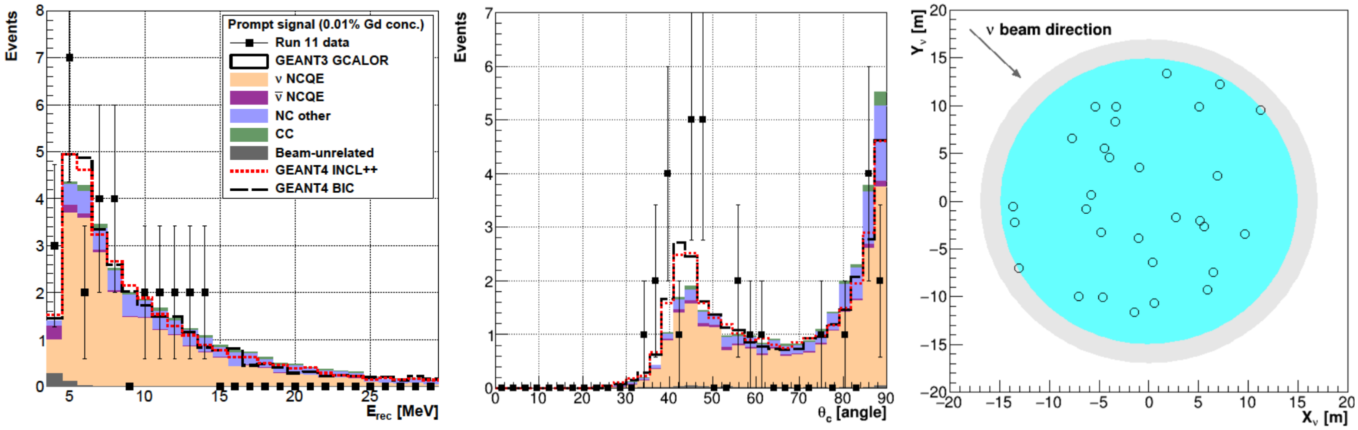

FIG. 4. Distributions of the reconstructed energy ($E_{\rm rec}$, left), Cherenkov angle ($\theta_{\rm C}$, middle), comparing data to MC prediction, and vertex position (right) for selected prompt events. The arrow in the right panel indicates the neutrino beam direction. The gray region marks the inner detector, and the blue region denotes the fiducial volume (top view).

TABLE II. Number of prompt event candidates surviving each selection step for the On-Beam and Off-Beam data, compared to various SI models predictions (GEANT3 GCALOR and three SI models from GEANT4). The selection efficiency for each MC prediction is shown in parentheses. Off-Beam event counts are rescaled to the On-Beam time window length to allow direct comparison, while beam-unrelated backgrounds are not simulated. The final row, $\rm N_{prompt}$, lists the number of prompt events passing all selections.

	Observed Data		Monte Carlo Simulation			
Selection	On-Beam	Off-Beam	GEANT3 GCALOR	GEANT4 BERT	GEANT4 INCL++	GEANT4 BIC
Timing	358	331.2	-	-	-	-
Decay-e	356	330.9	-	-	-	-
FV	92	67.4	35.9 (75.0%)	41.7(72.5%)	40.0(71.4%)	40.3(71.8%)
dwall	82	58.5	35.7 (74.6%)	41.5(72.1%)	39.8(70.9%)	40.0(71.4%)
effwall	60	34.7	35.3 (73.8%)	41.1(71.5%)	39.3(70.1%)	39.5(70.5%)
ovaQ	31	0.4	34.6 (73.7%)	39.5(68.7%)	37.5(66.9%)	37.8(67.4%)
CC interaction	30	0.4	31.5 (65.8%)	33.5(58.2%)	31.0(55.3%)	30.9(55.1%)
$N_{\rm prompt}$	30	0.4	31.5	33.5	31.0	30.9

1. $E_{\rm rec}$ selection: prompt events must have a reconstructed total energy, $E_{\rm rec}$, in the range [3.49, 29.49] MeV. The lower limit reflects the SK threshold, and the upper limit avoids Michel electron contamination.

2. Timing selection: the reconstructed event time must be within ±100 ns of the expected timing of a beam bunch.

3. Decay-e selection: events with more than 22 hits within a sliding 30 ns time window spanning 0.2 to 20 μs before the arrival time of the beam are rejected. This cut removes events created by the Michel electron from a preceeding muon or charged pion.

4. FV selection: prompt events must fall within the fiducial volume; the reconstructed vertex is required to be more than 200 cm away from any ID wall.

5. *dwall*, *effwall* and *ovaQ* selection: to suppress backgrounds from radioactive impurities near the detector wall, additional cuts were applied in the [3.49, 5.99] MeV reconstructed energy range. Cuts are based on three variables: the event's distance to the ID wall (*dwall*), the distance along the track to the ID wall (*effwall*), and the reconstruction quality (*OvaQ*) [57]. Specifically, the following conditions must be met:

$$dwall > p_0^{dwall} + p_1^{dwall} \times E_{\rm rec}, \tag{2}$$

$$effwall > p_0^{effwall} + p_1^{effwall} \times E_{\rm rec}, \tag{3}$$

$$OvaQ > p_0^{OvaQ} + p_1^{OvaQ} \times E_{\rm rec}, \tag{4}$$

where the parameters have been optimized and are set as $(p_0^{dwall}, p_1^{dwall}) = (580.0\ {\rm cm}, -80.0\ {\rm cm} \cdot {\rm MeV}^{-1})$, $(p_0^{effwall}, p_1^{effwall}) = (1941.5\ {\rm cm}, -314.0\ {\rm cm} \cdot {\rm MeV}^{-1})$ and $(p_0^{OvaQ}, p_1^{OvaQ}) = (0.4125, 0.042\ {\rm MeV}^{-1})$.

6. CC interaction selection: in order to remove CC

backgrounds, a cut on reconstructed energy and Cherenkov angle is applied. Events satisfying $\theta_C > a \times E_{\rm rec} + b$, are selected, where $a = 1.67$ deg $\cdot$ MeV^{-1} and $b = 15.0$ deg have been optimized using MC.

These selections are the same as those used in the past T2K NCQE analysis [4]. However, because the beam and detector conditions vary from run to run, the cut optimizations for criteria 5 and 6, based on SKDETSIM, have been updated in this study. We follow the procedure from the past T2K NCQE analysis to determine the cut parameters using a figure-of-merit (FOM), defined as:

$$\mathrm{FOM} = \frac{N_{\rm sig}}{\sqrt{N_{\rm sig} + N_{\rm bkg}}},$$

where $N_{\rm sig}$ represents the number of MC predicted ν-NCQE signal events, and $N_{\rm bkg}$ is the total background. The total background consists of non-signal neutrino events from MC (e.g., NC-other and CC interactions) and beam-unrelated background events from Off-Beam data.

MC events are weighted using the delivered POT, the energy-dependent neutrino flux, and the associated interaction cross section. Table II summarizes the prompt event selection for both data and MC. The final number of expected events from GEANT3 GCALOR (SKDETSIM) is 31.9, which includes the contribution from beam-unrelated backgrounds (0.4), and 30 events are observed in the data. The effectiveness of the reduction of beam-unrelated backgrounds can be seen through each selection stage in the Off-Beam column. After all selections, this background is reduced by about three orders of magnitude. Fig. 4 shows the $E_{\rm rec}$, θ_C, and vertex distribution of the prompt events. The observed $E_{\rm rec}$ distribution agrees well with the predictions, and the event vertices are uniformly distributed in the detector, as is expected. In the θ_C distribution, the data at $\sim 42^{\rm o}$ angles are above the MC expectation. A Kolmogorov-Smirnov test to the θ_C distribution yielded a p-value of 15%, indicating acceptable compatibility of the data and MC. Appendix B 2 provides a detailed look at the prompt events.

B. Delayed Signal Search

The delayed signal induced by a neutron capture is selected using an algorithm which consists of two stages: a pre-selection and a neural network (NN) classification. The pre-selection involves identifying PMT hit clusters that potentially represent neutron capture signals. Following this, the neural network classification is used to discriminate the neutron capture signal from accidental noise.

1. Pre-selection

Neutron candidates are searched for within [3, 500] μs time window following a prompt event. Hit clusters are formed by finding a cluster of PMT hits with a time-of-flight (ToF) correction based on the prompt event vertex, which is reconstructed with BONSAI. A 14 ns time window is employed for hit cluster searches, determined by the neutron capture time resolution and the optimization discussed in Ref. [58]. Hit clusters with the number of PMT hits ranging between 7 and 400 PMT hits, which correspond to reconstructed energies between approximately $\mathcal{O}(1) \sim \mathcal{O}(10)$ MeV, are classified as a neutron candidate. This energy range includes the total energy deposition expected from neutron capture on both gadolinium and hydrogen with some margin. For events with one or more than one such candidate, a search for additional neutron candidates is performed. Each additional candidate is required to be more than 200 ns apart from a previous candidate to avoid double counting hits from previous clusters. Fig. 5 illustrates the concept of this pre-selection.

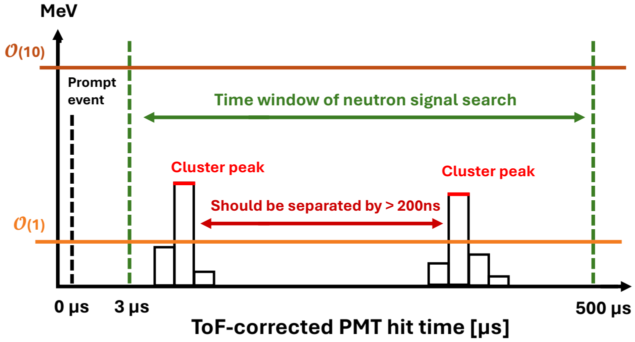

FIG. 5. Conceptual illustration of the neutron candidate pre-selection. PMT hits after each prompt event are grouped into ToF-corrected clusters within a [3, 500] μs window. Clusters with reconstructed energy in the $\mathcal{O}(1) \sim \mathcal{O}(10)$ MeV range are labeled as neutron candidates, with a minimum 200 ns gap to avoid double counting.

2. Neural network classification

Each neutron candidate passing the pre-selection is then subject to a NN classification to reduce accidental backgrounds which typically arise from PMT dark noise. The 14 ToF-corrected features were selected to capture key neutron candidate information and fall into five categories: hit-cluster size (Hits), timing spread relative to the vertex (Timing), vertex quality and position (Vertex), topological correlations expected from Cherenkov cone (Topology), and PMT dark-noise signatures (PMT Noise).

(1) Hits: two variables related to the number of PMT

hits, `NHits` and `NResHits`, are used. `NHits` denotes the number of PMT hits within a sliding time window with 14 ns width, with the window centered on the point of maximum hits. `NResHits` is the difference between the number of PMT hits taken in a larger window, [−100, +100] ns, and `NHits`.

(2) Timing: one variable related to the PMT timing, `TRMS`, is used. This parameter is the root-mean-square PMT hit time taken over all hits in the candidate's hit cluster.

(3) Vertex: three distributions related to the candidate's vertex, `FitGoodness`, `DWall` and `DWallMeanDir` are used. `FitGoodness` represents the quality of vertex reconstruction, based on the timing likelihood calculated by the reconstruction algorithm, assuming a PMT timing resolution of 5 ns. `DWall` represents the shortest distance from the reconstructed vertex to any ID wall, and `DWallMeanDir` is the distance along the mean direction from the neutron candidate's vertex to each hit PMT.

(4) Topology: several parameters related to the spatial distribution of hits in the detector are used, `Beta`(k) with $k \in \{1, 2, 3, 4, 5\}$ and `OpeningAngleStdev`. The `Beta`(k) parameters are defined as

$$\texttt{Beta}(k) \equiv \frac{2}{\texttt{NHits}\,(\texttt{NHits}-1)} \sum_{i \neq j} P_k\left(\cos\theta_{ij}\right), \qquad (5)$$

where $\mathrm{P}_k(\cos\theta_{ij})$ is the k-th degree Legendre polynomial, and θ_{ij} represents the angle between a pair of PMT hits as viewed from the neutron candidate's reconstructed vertex. `OpeningAngleStdev` represents the standard deviation of the observed angle among triplets of hit PMT recorded within a 14 ns time window.

(5) PMT Noise: two parameters related to the intrinsic noise characteristics of the PMT are used, `DarkLikelihood` and `BurstRatio`. `DarkLikelihood` expresses the likelihood that the PMT hits were caused by dark noise and is calculated based on the measured dark rates of the individual hit PMT. `BurstRatio` represents the ratio of PMT hits occurring in 10 μs prior to the neutron candidate relative to the total number of hits from the candidate. This parameter is used to separate neutron-induced hits from those created by scintillation light from particles emitted by radioactive impurities in the PMT glass.

The feed-forward fully connected NN was trained and calibrated using a ^{241}Am/Be neutron source and beam-unrelated background as described in Ref. [58]. Fig. 6 shows the likelihood output of neutron candidates from the beam data and MC. A neutron candidate is classified as a delayed signal if its likelihood output exceeds 0.7, achieving approximately 99% neutron purity with the accidental noise rate per selected prompt event (η_{Noise}) around 1%. The η_{Noise} is calculated using the data set collected in the Off-Beam time window. Fig. 7 illustrates the 14 features of the delayed signals after the NN selection cut is applied. Overall, the neutron detection algorithm achieves a neutron detection efficiency (ϵ_{n}) of 43.1% from MC, as summarized in Table III.

TABLE III. Summary of the neutron detection algorithm for neutron detection efficiency, accidental noise rate, and purity.

	n detection algo.	
	H(n,γ)	Gd(n,γ)
neutron detection efficiency	3.1%	40.0%
	Overall	
neutron detection efficiency (ϵ_{n})	43.1%	
Acc. noise rate (η_{Noise})	1.3%	
Purity	98.7%	

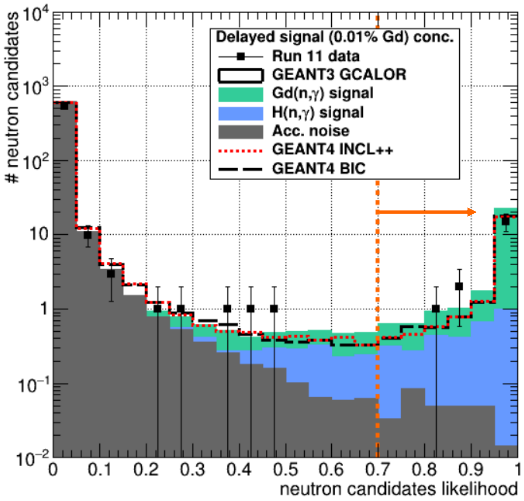

FIG. 6. The likelihood distribution of all neutron candidates from beam neutrino events, determined by the neural network. Neutron candidates with likelihood values above 0.7 are defined as "delayed" signals, matching the delayed signal counts in Table IV, and yield approximately 99% purity with about 1% accidental noise.

The results of the delayed signal search are summarized in Table IV. The N_{delayed} row represents the total number of delayed signals observed among the total number of prompt events, N_{prompt}, shown in Table II. The number of expected delayed signals is 30.8, while 18 are observed. The alternative SI models, INCL++ and BIC, predict a lower number than the BERT model, consistent with the NCQE study from atmospheric neutrinos in SK [6].

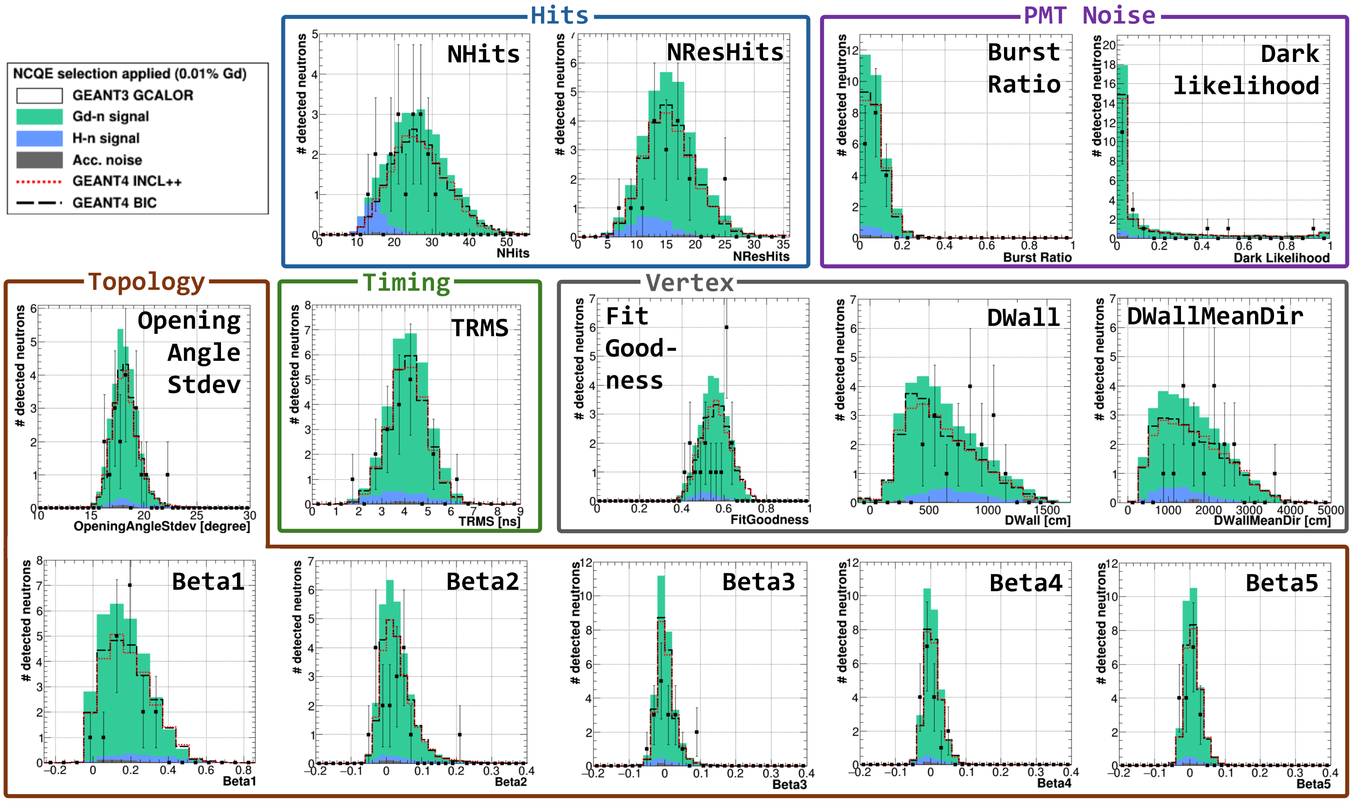

FIG. 7. Comparison of the 14 input features of the delayed signals for the data set and MC prediction in the neural network classification.

TABLE IV. Delayed signal numbers from the data set and MC are presented. Detector simulations with different SI models are provided, and ratios of each interaction channel to total signals are shown in parentheses. The data set is categorized into On-Beam and Off-Beam, where Off-Beam assesses accidental noise.

	Observed Data		Monte Carlo simulation			
Channel	On-Beam	Off-Beam	GEANT3 GCALOR	GEANT4 BERT	GEANT4 INCL++	GEANT4 BIC
ν-NCQE	-	-	19.3 (62.6%)	17.9 (53.8%)	12.9 (51.8%)	13.0 (51.6%)
$\bar{\nu}$-NCQE	-	-	0.5 (1.6%)	0.5 (1.5%)	0.4 (1.5%)	0.4 (1.5%)
NC-other	-	-	9.5 (30.9%)	9.4 (28.2%)	7.0 (28.2%)	7.1 (28.2%)
CC	-	-	1.1 (3.7%)	4.6 (13.9%)	3.9 (15.5%)	4.0 (15.8%)
Noise	-	0.3 (1.7%)	0.4 (1.2%)	0.9 (2.6%)	0.8 (3.0%)	0.8 (2.9%)
N_{delayed}	18		30.8	33.3	25.0	25.3

V. RESULT

This analysis measures the mean neutron capture multiplicity, M, using the formula:

$$M = \frac{(N_{\text{delayed}} - \eta_{\text{Noise}} \times N_{\text{prompt}})/\epsilon_n}{N_{\text{prompt}}}. \quad (6)$$

The calculation begins with the number of delayed signals (N_{delayed}). Since the observed N_{delayed} includes mistagged neutrons from accidental noise, its subtraction is required. For the data set, this is determined from the number of signals in the Off-Beam window, while for the MC, the number of mistagged neutrons is calculated by multiplying the accidental noise rate (η_{Noise}) by the number of prompt events (N_{prompt}). After this subtraction the number of delayed signals is then corrected by the neutron detection efficiency (ϵ_n). Finally, the corrected number of delayed signals is divided by the number of prompt events (N_{prompt}) to obtain M.

The following sections present systematic uncertainties associated with the components of Eq. (6).

A. Systematic Uncertainty of ϵ_n

The neutron detection efficiency, ϵ_n, is determined from simulations and is therefore subject to several modeling uncertainties, which are summarized in Table V. Among them, the detector response for the delayed signal is the dominant source, followed by those stemming from the prompt event selection and the nucleon SI model. These three are discussed below, while detailed evaluations for the other error sources can be found in Appendix A.

TABLE V. Summary of the uncertainties contributing to the neutron detection efficiency (ϵ_n). The dominant contribution arises from the detector response to delayed signals, while other sources introduce relatively smaller uncertainties.

	Uncertainty of ϵ_n
Detector response to delayed signal	+5.3%/–8.1%
Nucleon SI	+0.0%/–0.8%
Prompt signal selection	±0.5%
MC statistics	±0.1%
ν beam flux	±0.4%
ν oscillation	±0.01%
ν interaction	±0.4%
π capture on ^{16}O	+0.0%/–1.5%
μ capture on ^{16}O	+0.0%/–0.5%
PMT gain	negligible
Water status	negligible
Total	+5.4%/–8.4%

1. Detector response to the delayed signal

The uncertainty in the detector response to the delayed signal is assessed using a ^{241}Am/Be neutron source. The most critical factors are the H(n, γ) (Gd(n, γ)) capture ratio, $r_{\mathrm{H}}(r_{\mathrm{Gd}})$, the probability for thermal neutrons to be captured on hydrogen (gadolinium) and the accuracy of the gadolinium interaction modeling.

We find that the ^{241}Am/Be MC simulation underestimates the r_{H} compared with the calibration result. By examining the PMT-hit distribution, we obtain a χ^2-fitted r_{H} of 56±3%, which is consistent with the analytically predicted value of 56.2±1.5% from ENDF/B-VII.1. In contrast, the ^{241}Am/Be MC simulation predicts a lower value, 48% for r_{H} [58]. The underestimation of r_{H} occurs because the GEANT4 Neutron High-Precision model currently treats hydrogen as a free nucleus rather than accounting for water's molecular mass. As a result, hydrogen is simulated to move 18 times faster, reducing the probability of neutron capture on hydrogen and thus lowering the r_{H} [59]. Since the re-calibration and further investigations of GEANT3 are still on-going, this analysis uses the existing default settings. After combining calibration and cross section uncertainties, we obtain r_{H} with a central value of $48^{+8.2}_{-1.5}$%, and this uncertainty carries over to the r_{Gd} because $r_{\mathrm{Gd}} \approx 1 - r_{\mathrm{H}}$. The ϵ_n is obtained by adding the hydrogen contribution, given by the product of r_{H} and detection efficiency on hydrogen, to the gadolinium contribution, defined analogously. Propagating these correlated uncertainties yields an overall neutron detection efficiency of $43.1^{+1.3}_{-6.1}$% in this study. Table VI summarizes the uncertainty of ϵ_n related to the detector response to N_{delayed}.

TABLE VI. Summary of systematic uncertainties of ϵ_n introduced by the detector response to the delayed signal. The table is derived from ^{241}Am/Be neutron source calibration, encompassing neutron kinetic energy, detector, and Gd modeling [58]

.

Source type	Source name	Uncertainty of ϵ_n
AmBe neutron modeling	1. neutron kinetic energy	±0.3%
Detector modeling	2. Time evolution of detector characteristics	±0.6%
	3. PMT quantum efficiency	±0.4%
Gd modeling	4. Gd/H-capture ratio	+1.3%/–6.1%
	5. Gd-capture γ model	±5.1%
	Total	+5.3%/–8.1%

2. Prompt event selection

The systematic uncertainty on ϵ_n due to the prompt event selection includes contributions from cuts on E_{rec}, θ_{C}, *dwall*, *effwall*, and *OvaQ* [57], all of which carry uncertainties originating from the detector response and reconstruction. The uncertainties associated with E_{rec}, *OvaQ*, and θ_{C} are 5%, 1.5%, and 2 degrees, respectively [45]. In addition, the uncertainties concerning *dwall* and *effwall* are derived from the vertex resolution. The uncertainties in the vertex resolution along radial (R_ν) and vertical (Z_ν) directions are 10 cm and 5 cm, respectively [45]. Accordingly, the prompt event selection introduces an uncertainty of 0.5% on ϵ_n.

3. Nucleon SI

SI models differ in their adopted interaction cross sections and in their predictions of the outgoing nucleon kinematics, which may introduce a systematic uncertainty on ϵ_n and impact the prediction of neutron multiplicity. In GEANT3 GCALOR, the overall cross section in the energy range of interest is calculated based on nucleon-nucleon scattering cross sections [24]. An uncertainty of 30% was assigned to this total cross section following Ref. [60], which compared the measured p-^{12}C scattering cross sections with several theoretical predictions. Notably, the prediction computed using the same nucleon SI cross sections adopted in this study agreed with the world experimental data on proton-carbon scattering to within 30%, thus supporting the assigned error.

In GEANT4, the uncertainty can be evaluated by performing the analysis using different SI models. Since GEANT3 GCALOR is based on the BERT model, we continue to use GEANT4 BERT as our basis for the GEANT4 analysis and estimate uncertainties by changing to the INCL++ and BIC models.

The uncertainty from the choice of SI model on ϵ_n is taken to be the largest change in detection efficiency among these models, $\Delta\epsilon_{\mathrm{SI}}$ and estimated to be $^{+0.0\%}_{-0.8\%}$. Table VII summarizes the neutron detection efficiency, ϵ_n, associated with the choice of SI model, along with the variations in the predicted number of delayed signals.

TABLE VII. Change in detection efficiency, ϵ_n, introduced by SI models with GEANT3 GCALOR and GEANT4 (BERT, INCL++, BIC). The neutron detection efficiency variation $\Delta\epsilon_{\mathrm{SI}}$ is calculated by comparing the nominal to regenerated MC samples. The uncertainty in the predicted number of delayed signals is also summarized here.

	GEANT3			GEANT4		
	−30%	GCALOR	+30%	INCL++	BERT	BIC
ϵ_n	42.3%	43.1%	42.7%	41.2%	41.5%	41.3%
$\Delta\epsilon_{\mathrm{SI}}$	−0.8%	-	−0.4%	−0.3%	-	−0.2%
N_{delayed}	28.4	30.8	31.6	25.0	33.3	25.3
$\Delta N_{\mathrm{delayed}}$	−7.9%	-	+2.5%	−24.9%	-	−24.0%

B. Mean Neutron Capture Multiplicity and Neutron Features

The measured mean neutron capture multiplicity is:

$$M_{\mathrm{data}} = 1.37 \pm 0.33\,(\mathrm{stat.})^{+0.17}_{-0.27}\,(\mathrm{syst.}) \tag{7}$$

The expectations extracted from MC with different SI models are as follows:

$$M_{\mathrm{MC}}(\text{GEANT3 GCALOR}) = 2.24 \pm 0.01\,(\mathrm{stat.}) \tag{8}$$
$$M_{\mathrm{MC}}(\text{GEANT4 BERT}) = 2.28 \pm 0.01\,(\mathrm{stat.}) \tag{9}$$
$$M_{\mathrm{MC}}(\text{GEANT4 INCL}++) = 1.84 \pm 0.01\,(\mathrm{stat.}) \tag{10}$$
$$M_{\mathrm{MC}}(\text{GEANT4 BIC}) = 1.87 \pm 0.01\,(\mathrm{stat.}) \tag{11}$$

Fig. 8 compares the mean neutron capture multiplicities obtained from this study with these expectations, while Fig. 9 shows the neutron capture multiplicity distribution. Note that all models overpredict the neutron multiplicity by at least 1σ compared to the data.

Scaling the nominal SI cross section by 30% induces at most a 7.9% change in the predicted number of delayed signals (c.f. Table VII), while changing the SI model in GEANT4 leads to about a 25% variation. Uncertainties from other potential factors are also outlined in Table VIII, but none has as significant an impact as the SI models in GEANT4. This result shows a slight preference for GEANT4 INCL++ and BIC models, as they better reproduce the observed multiplicity and yield a lower χ^2 value, as shown in Fig. 9.

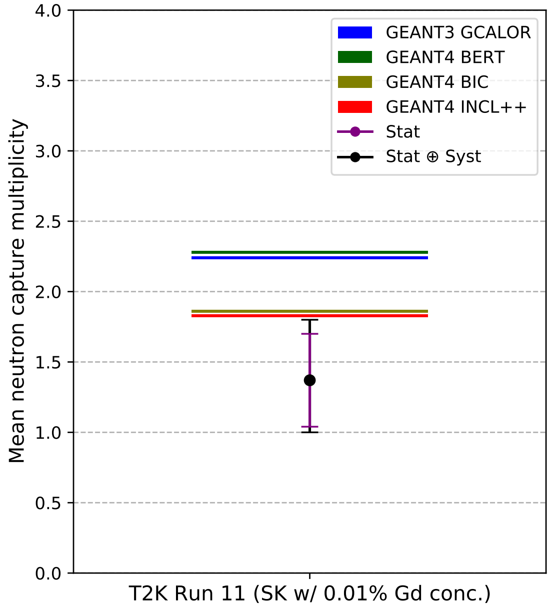

FIG. 8. Comparison of the measured mean neutron capture multiplicity to MC predictions using different SI models. The inner and outer error bars represent systematic and total uncertainties, respectively.

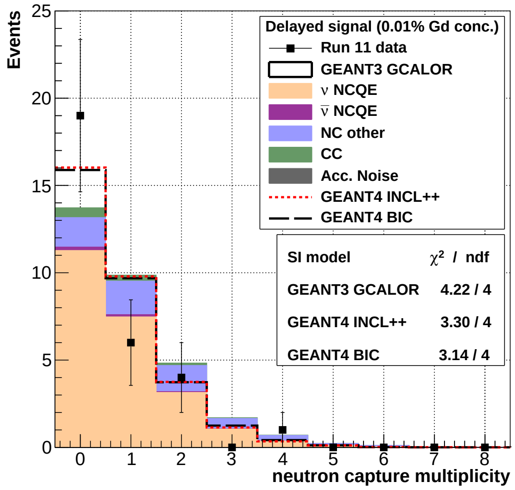

FIG. 9. Neutron capture multiplicity distribution for data compared to MC predictions with different SI models.

The left plot of Fig. 10 presents the measured neutron capture time, while the center plot of Fig. 10 depicts the neutron travel distance, which is defined as the distance between the reconstructed prompt and delayed signal vertices. Although both figures demonstrate overall agreement between the data and MC, two delayed sig-

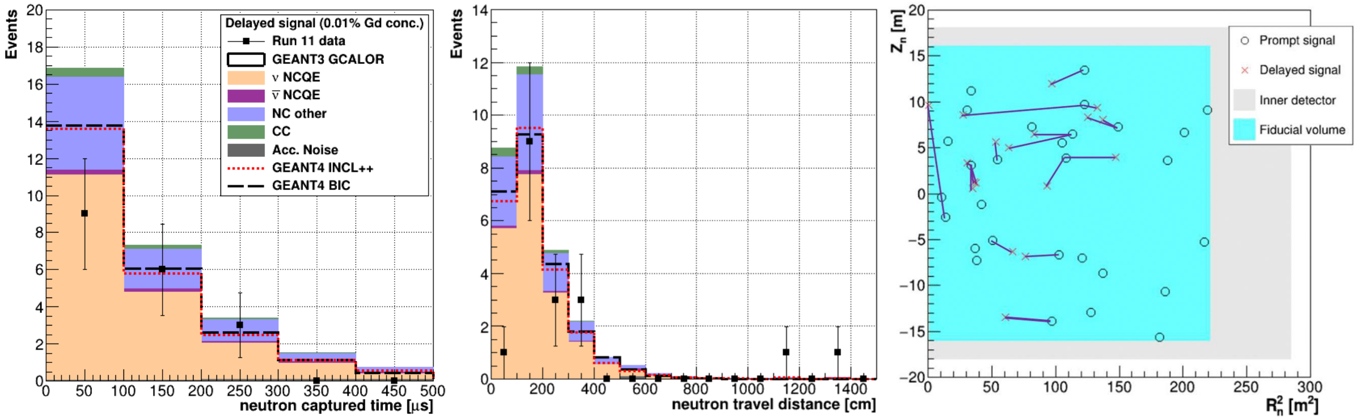

FIG. 10. Neutron capture time (left) and neutron travel distance (center) for data compared to MC predictions with different SI models. The right panel presents the two-dimensional distribution of NCQE-like events, with purple lines connecting each prompt event (circle) to its corresponding delayed signals (cross).

nals with travel distances more than 700 cm are observed though 0.5 signals are expected in this region.

One of the delayed signals could be attributed to accidental noise, estimated at 0.4 signals in this study. For signals beyond 700 cm, the Poisson probabilities of detecting 0, 1, or 2 neutrons are 60.7%, 30.3%, and 7.6%; the corresponding noise probabilities are 67.0%, 26.8%, and 5.4%. Combining these gives 9% for one neutron plus one noise event. However, we note that neutron travel distance is longer in data than in MC as indicated by the mismatch in the [0, 100] cm bin. Variation among SI models, which modify the neutron momentum spectra and consequently the predicted travel distances, does not fully explain this discrepancy.

Finally, the right plot of Fig. 10 shows the vertex distributions of selected prompt events and delayed signals with lines connecting the two when both exist.

VI. DISCUSSION

Given the deficit of observed data relative to MC predictions for the number of delayed signals, we discuss the influence of modeling choices on those predictions. While other modelling aspects affect the prediction to a lesser extent than the adoption of SI model discussed above, we find that contributions for modeling of short-range nucleon correlations, NC 2p2h interactions, and the strange coupling constant induces a roughly 10% variation. Other nuclear modelling, such as Pauli blocking and nuclear de-excitation processes, were found to have a minor impact. Table VIII provides a summary of the delayed signal prediction variations from these studies.

A. Short-Range Correlations

The spectral function by Benhar et al. [31] includes both mean-field and short-range correlations (SRC). SRC refers to the strong, localized interactions between pairs of nucleons within a nucleus. Under the influence of SRC, a neutrino NCQE-like interaction can result in two outgoing nucleons from the primary interaction, both of which can go on to generate secondary neutrons via SI. NEUT and NuWro choose different SRC regions in the spectral function [64], which may lead to different neutron predictions. Switching to events generated with NuWro (version 21.09), but propagated with the same SI model as the nominal analysis, yields the neutron multiplicity distribution shown in Fig. 11. This change results in an overall increase of 9.4% in the predicted number of neutrons.

B. NC 2p2h

In the hypothesis of NC 2p2h interactions, both outgoing hadrons could lead to the production of neutrons in the final state, thereby changing the predictions used in this study. NEUT uses the Valencia 2p2h model by Nieves et al. [34], which does not include NC 2p2h interactions. In order to estimate the potential impact of adding the NC channel, we study the TEM model [62] from NuWro. The NuWro TEM model allows for the simulation of both CC and NC 2p2h interactions via the adjustment of vector magnetic form factors. Importantly, the NC channel can be suppressed in the simulation. NuWro's predictions for the neutron capture multiplicity distribution with and without the NC 2p2h interaction are shown in Fig. 12 as dashed red and dotted blue lines, respectively. NEUT's prediction is depicted as a solid black line. The number of delayed signals resulting from NC 2p2h interactions in the TEM constitutes an

TABLE VIII. Summary of the delayed signal variations under different conditions beyond the SI models.

Factors	$\Delta N_{\mathrm{delayed}}$	Reference setting
Nominal setting	-	NEUT w/ GEANT3 GCALOR
Short-Range Correlations	+9.4%	NuWro [61]
NC 2p2h	+12.0%	NuWro w/ TEM model [62]
$g^{\mathrm{s}}_{\mathrm{A}}$	−9.0%	NuWro w/ $g^{\mathrm{s}}_{\mathrm{A}} = -0.3$
Pauli Blocking	−0.5%	NEUT w/ PB
Deexcitaion in ν-^{16}O NCQE	+0.9%	NEUT w/ NucDeEx [63]
GEANT3 SI model	−7.9%/+2.5%	NEUT w/ GEANT3 GCALOR ±30% Xsec
GEANT4 SI models	−25.6%	NEUT w/ GEANT4 INCL++

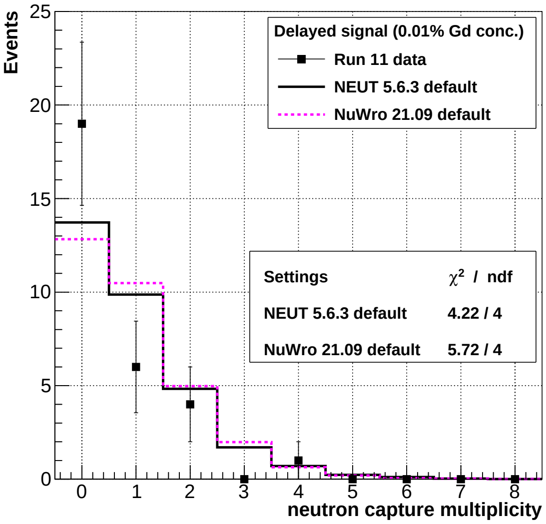

FIG. 11. The neutron capture multiplicity with NEUT default (black) and NuWro 21.09 default (red) is shown. NuWro predicts 9.4% more neutrons than NEUT, which is a minor impact when compared to SI models.

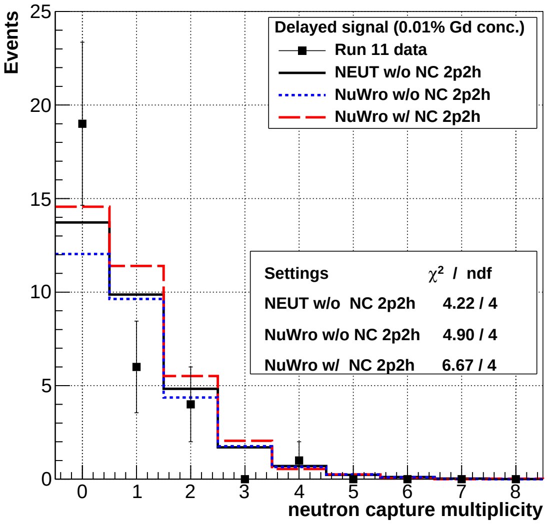

FIG. 12. The neutron capture multiplicity with the default NEUT prediction is represented by a black solid line. The NuWro predictions using the TEM model [62], with and without NC 2p2h interactions, are shown in red and blue dashed lines, respectively. When comparing the scenarios with and without the NC 2p2h interaction, there is an approximate 12% increase in neutron prediction.

approximately 12% increase. For this comparison, the default value of the fraction of *np* pairs, 85^{+15}_{-20}%, was used. The fractions of *pp* and *nn* pairs, which share the same isospin, are roughly equivalent.

C. Strange Axial Coupling Constant

The neutron capture multiplicity could also be affected by the strange axial coupling constant ($g^{\mathrm{s}}_{\mathrm{A}}$), which quantifies the contribution of strange quark-antiquark pairs to the nucleon's spin. NC processes involving the axial current could be influenced by $g^{\mathrm{s}}_{\mathrm{A}}$, and we focus on NCQE as it is the dominant contribution in this study. A negative $g^{\mathrm{s}}_{\mathrm{A}}$ value enhances the NCQE cross section on protons but reduces it on neutrons [65]. Since NCQE interactions with protons seldom result in neutron emission, they generally lead to events with zero neutron capture multiplicity. As a result, a negative $g^{\mathrm{s}}_{\mathrm{A}}$ is expected to reduce the mean neutron capture multiplicity for NCQE interactions.

A negative $g^{\mathrm{s}}_{\mathrm{A}}$ means strange-quark spins anti-align with up/down quarks, lowering the nucleon's total spin. Investigations of $g^{\mathrm{s}}_{\mathrm{A}}$ using the NCQE interaction have been conducted in experiments such as BNL E734 [66], MiniBooNE [67] and KamLAND [65], all of which favor negative values. NEUT version 5.6.3 uses $g^{\mathrm{s}}_{\mathrm{A}} = 0$ and does not support modifications to this parameter. In contrast, NuWro allows for the direct input of $g^{\mathrm{s}}_{\mathrm{A}}$. Here we use NuWro and scan $g^{\mathrm{s}}_{\mathrm{A}}$ from 0.0 to −0.3 to cover the majority of existing measurements from both neutrino and electron scattering experiments [68–71], with −0.3 serving as a conservative lower bound. Other generator settings are kept at their default values to evaluate the effect of $g^{\mathrm{s}}_{\mathrm{A}}$ on the neutron capture multiplicity.

Fig. 13 shows the expected neutron capture multiplicity results for different $g^{\mathrm{s}}_{\mathrm{A}}$ values from NEUT and NuWro. The black line in Fig. 13 represents the default $g^{\mathrm{s}}_{\mathrm{A}}$ value

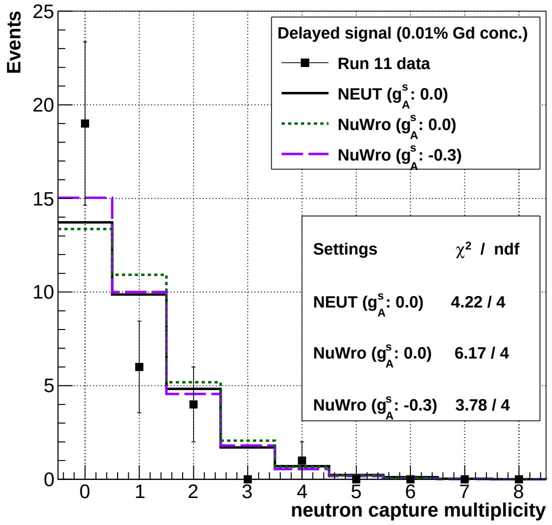

FIG. 13. The neutron capture multiplicity with the default g_A^s value in NEUT is represented by a black solid line. The NuWro predictions, with the default g_A^s value, 0.0, and the average values of existence g_A^s measurement, −0.3, are shown in green dotted and purple dashed lines, respectively. When comparing the scenarios $g_A^s = -0.3$ to $g_A^s = 0.0$ within NuWro, there is an approximate 9% decrease in the delayed signal prediction.

from NEUT, set at 0.0. The dotted green line indicates $g_A^s = 0.0$, the default value in NuWro. Finally, the dashed purple line represents $g_A^s = -0.3$. Setting g_A^s to −0.3 reduces the predicted number of neutrons by 9% compared to NuWro's default.

D. Pauli Blocking

The SF model [31, 32] adopted in NEUT 5.6.3 does not consider Pauli blocking. We therefore enforce it manually to estimate its impact on this analysis. Following the prescription in Ref. [72], the cross section is set to zero in regions of phase space where, prior to undergoing FSI, the momentum of the outgoing primary nucleon falls below the Fermi momentum. Accordingly, this approach reduces the overall cross section and additionally results in a change in its shape at low momentum transfer. Fig. 14 shows the neutron capture multiplicity prediction with (brown dotted line) and without (black) Pauli blocking enforced. Enabling Pauli blocking reduces the total neutron count by approximately 0.5%, with predictions remaining nearly identical to the default. However, a decrease in the zero-neutron capture multiplicity is observed, suggesting a slight increase in the mean neutron capture multiplicity.

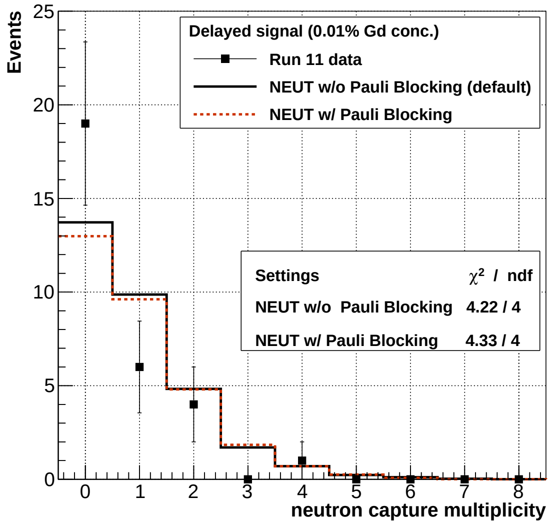

FIG. 14. The neutron capture multiplicity with and without Pauli blocking is shown as a black solid line and a brown dotted line, respectively. In this study, NEUT with Pauli blocking predicts approximately a 0.5% reduction in the number of delayed signals compared to NEUT without Pauli blocking, which serves as the default.

E. Nuclear De-excitation in Neutrino Interaction

The choice of nuclear de-excitation model can also cause variations in the total number of predicted neutrons. NEUT adopts a data-driven model [40], but we additionally consider the NucDeEx [63, 73] (version 1.0) model for an alternative estimate of the hadrons and photons produced during nuclear de-excitation. NucDeEx employs the nuclear reaction simulator TALYS version 1.96 [74] for the de-excitation calculation following a neutrino interaction with ^{16}O. TALYS has access to more recent, precise, complete data [75] than the model used in NEUT. For this comparison, only ν-NCQE interactions were considered in this study due to the limitations in NucDeEx. Fig. 15 shows the neutron capture multiplicity with and without NucDeEx. The simulation with NucDeEx resulted in a 5.1% increase in the total number of generated neutrons compared to the case with the NEUT default de-excitation model without any selections. We noticed that the additional neutrons introduced by NucDeEx mostly occur in prompt events below 5 MeV, which is the main reason most of these neutrons are not retained. The relatively low energy of prompt events causes a significant loss of additional neutrons, both through the energy threshold applied in prompt event selection and through imprecise TOF corrections stemming from the relatively large vertex resolution during the pre-selection stage. Overall, the full simulation with NucDeEx predicts a 0.9% increase in the number of delayed signals relative to the nominal model.

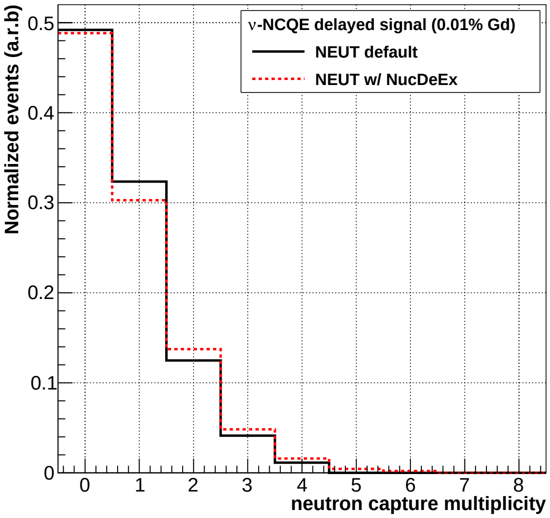

FIG. 15. The neutron capture multiplicity predictions with (red dotted line) and without (black solid line) NucDeEx are shown. The delayed signals prediction presented here are from ν-NCQE interactions. NEUT with NucDeEx predicts a 0.9% increase in delayed signals compared to the default de-excitation model in NEUT.

F. Insights from Other Neutrino-induced Neutron Measurements

So far, only a few measurements of neutrons associated with neutrino interactions have been conducted. The T2K [76], ANNIE [77], MINERνA [78] and SNO [79] collaborations have all observed an overprediction of the neutron (capture) multiplicity with either beam or atmospheric neutrinos. These results collectively indicate that simulation settings with BERT-based models, which are used in these experiments, tend to overpredict the neutron (capture) multiplicity, while KamLAND [65], whose simulation is based on the BIC model, does not see such an overprediction. Given the wide range of energies spanned by these experiments, from MeV to GeV, neutron overprediction observed in both the CCQE and NCQE channels may hint at a connection to FSI modeling. However, as demonstrated above, the effect of SI modeling appears to dominate. SK [6] similarly tested several SI models, including BERT, INCL++, and BIC, using atmospheric neutrino NCQE events and reached a similar conclusion: BERT tends to overpredict, whereas INCL++ and BIC provide more accurate predictions for neutron capture multiplicity. One of the main reasons is that BERT used the de-excitation model native to the Bertini code, while others use the G4PreCompound model [26]. As described in Ref. [53], the G4PreCompound model relies on an exciton-based pre-equilibrium approach followed by semi-classical de-excitation mechanisms (e.g., Weisskopf-Ewing [80] or GEM [81]) once the nucleus reaches equilibrium, which provides higher accuracy for lower-energy processes but requires more computational time.

G. Prospects

A precise understanding of NCQE interactions and their final state particles is essential for DSNB searches at SK, Hyper-Kamiokande [82] and JUNO [83], as these detectors rely on neutron information to effectively reduce atmospheric NCQE backgrounds. In addition, improving our understanding of NCQE events is essential for dark matter [84, 85] and sterile neutrino search [86–88] in accelerator neutrino experiments, which further motivates improvements to measurements such as this work.

The statistical uncertainty on this measurement is expected to improve in the foreseeable future, as the anticipated POT proposed by T2K [89] has not yet been reached.

Furthermore, T2K data collected during the pure water [90] and 0.03% gadolinium [91] phases of SK could enhance the available statistics, providing roughly 10 times the neutron statistics used in this study. Understanding secondary interactions then becomes essential to reduce uncertainties in this measurement. Indeed, despite better data-MC compatibility in the current measurement when switching to the INCL++ and BIC models, there is still room for improvement.

While RCNP [92–94] and the ChipIr beamline at the Rutherford Appleton Laboratory [95] provide γ measurements from SI, there remains a lack of neutron measurements from SI. An inverse-kinematics experiment using an oxygen beam at RIKEN-RIBF and the SAMURAI spectrometer [96] can address this gap. We anticipate that SI models will be better constrained in the near future by such measurements. Dedicated upgrades to the GEANT4-based simulation may help reduce uncertainties on the neutron multiplicity and detection efficiency. The flexibility of GEANT4 allows users to customize the physics list based on the SI measurement mentioned above, offering the potential to enhance neutron kinematics predictions. A further dedicated calibration on the neutron capture, including the modification of GEANT4 secondary interaction model, could further minimize uncertainties. While experiments like NINJA [97] can help confirm CC 2p2h, direct measurements of NC 2p2h are an important missing piece. Electron scattering experiments, such as those at Jefferson Lab [98], provide precise data on nucleon momentum distributions and could potentially improve short-range correlation modeling. These efforts will assist precise measurements of the strange axial coupling constant with neutrino sources, ultimately enhancing the accuracy of NCQE interactions.

VII. CONCLUSION

In this paper we presented the first measurement of neutron capture multiplicity resulting from ν-^{16}O NCQE-like interactions, based on a data set corresponding to 1.76 × 10^{20} POT using the T2K neutrino beam. The observed mean neutron capture multiplicity was 1.37 ± 0.33 (stat.)$^{+0.17}_{-0.27}$ (syst.). The measurement deviates from the prediction made by NEUT combined with the Bertini-based SI model (2.24 ± 0.01 (stat.)). However, the predictions using other SI models, INCL++ (1.84 ± 0.01 (stat.)) and BIC (1.87 ± 0.01 (stat.)), are in closer agreement with the data. We found that SI modeling dominates the uncertainty in the predicted numbers of neutrons, compared to modeling of processes, such as short-range correlations, NC 2p2h interactions, the strange axial coupling constant, Pauli blocking, and nuclear de-excitation following the neutrino interaction. Similar neutron overprediction has been observed in experiments using BERT-based SI models in both the CCQE [76–79] and NCQE [6] channels, that is not observed in measurements using BIC model [65]. This work and these measurements highlight the need for a more precise understanding of SI processes and show that more data are needed to assess discrepancies and their origin. Despite the current uncertainties, the neutron detection efficiency of NCQE-like events estimated in this study can be utilized in atmospheric neutrino studies, for example, by accounting for the flux differences between T2K and atmospheric neutrinos. Further, the results of this study will serve as an essential validation tool for DSNB studies at water Cherenkov detectors, which aim to reduce atmospheric NCQE backgrounds using neutron information.
The data related to this work can be found in Ref. [99].

ACKNOWLEDGEMENT

The T2K collaboration would like to thank the J-PARC staff for superb accelerator performance. We thank the CERN NA61/SHINE Collaboration for providing valuable particle production data. We acknowledge the support of MEXT, JSPS KAKENHI (JP16H06288, JP18K03682, JP18H03701, JP18H05537, JP19J01119, JP19J22440, JP19J22258, JP20H00162, JP20H00149, JP20J20304, JP24K17065) and bilateral programs (JPJSBP120204806, JPJSBP120209601), Japan; NSERC, the NRC, and CFI, Canada; the CEA and CNRS/IN2P3, France; the Deutsche Forschungsgemeinschaft (DFG, German Research Foundation) 397763730, 517206441, Germany; the NKFIH (NKFIH 137812 and TKP2021-NKTA-64), Hungary; the INFN, Italy; the Ministry of Science and Higher Education (2023/WK/04) and the National Science Centre (UMO-2018/30/E/ST2/00441, UMO-2022/46/E/ST2/00336 and UMO-2021/43/D/ST2/01504), Poland; the RSF (RSF 24-12-00271) and the Ministry of Science and Higher Education, Russia; MICINN (PID2022-136297NB-I00 /AEI/10.13039/501100011033/ FEDER, UE, PID2021-124050NB-C31, PID2020-114687GB-I00, PID2019-104676GB-C33), Government of Andalucia (FQM160, SOMM17/6105/UGR) and the University of Tokyo ICRR's Inter-University Research Program FY2023 Ref. J1, and ERDF and European Union NextGenerationEU funds (PRTR-C17.I1) and CERCA program, and University of Seville grant Ref. VIIPPIT-2023-V.4, and Secretariat for Universities and Research of the Ministry of Business and Knowledge of the Government of Catalonia and the European Social Fund (2022FI_B 00336), Spain; the SNSF and SERI (200021_185012, 200020_188533, 20FL21_186178I), Switzerland; the STFC and UKRI, UK; the DOE, USA; and NAFOSTED (103.99-2023.144,IZVSZ2.203433), Vietnam. We also thank CERN for the UA1/NOMAD magnet, DESY for the HERA-B magnet mover system, the BC DRI Group, Prairie DRI Group, ACENET, SciNet, and CalculQuebec consortia in the Digital Research Alliance of Canada, and GridPP in the United Kingdom, and the CNRS/IN2P3 Computing Center in France and NERSC (HEP-ERCAP0028625). In addition, the participation of individual researchers and institutions has been further supported by funds from the ERC (FP7), "la Caixa" Foundation (ID 100010434, fellowship code LCF/BQ/IN17/11620050), the European Union's Horizon 2020 Research and Innovation Programme under the Marie Sklodowska-Curie grant agreement numbers 713673 and 754496, and H2020 grant numbers RISE-GA822070-JENNIFER2 2020 and RISE-GA872549-SK2HK; the JSPS, Japan; the Royal Society, UK; French ANR grant number ANR-19-CE31-0001 and ANR-21-CE31-0008; and Sorbonne Université Emergences programmes; the SNF Eccellenza grant number PCEFP2_203261; the VAST-JSPS (No. QTJP01.02/20-22); and the DOE Early Career programme, USA. For the purposes of open access, the authors have applied a Creative Commons Attribution license to any Author Accepted Manuscript version arising.

Appendix A: Uncertainties on Neutron Detection Efficiency

1. Statistical uncertainty

Statistical uncertainty in the neutron detection efficiency stems from the finite size of the MC and is estimated as ±0.1%. Similarly, the accidental noise rate carries a ±2.5% statistical uncertainty due to the limited size of the Off-Beam data set.

2. Neutrino beam flux

Neutrino beam flux uncertainties may cause variations in the types of neutrino interactions occuring in the detector, which subsequently affects our neutron detection efficiency. These uncertainties are evaluated for each flavor, energy, and horn polarity [19]. Hadron production and interaction modeling account for ∼8% around the flux peak, which represents the largest source. This study estimates the neutrino beam flux uncertainty in the same manner as the previous T2K analysis [4], resulting in a ±0.4% uncertainty on the neutron detection efficiency.

3. Neutrino oscillation

Uncertainties in oscillation parameters can affect the sample composition and, in turn, the neutron detection efficiency. The oscillation parameters and their associated uncertainties are sourced from Ref. [100]. Accounting for these errors induces only a ±0.01% uncertainty on the neutron detection efficiency since only CC events experience an observable oscillation effect.

4. Neutrino interaction model

The parameters and errors that describe the neutrino interaction cross sections and their values are taken from Ref. [101]. The value of the axial-vector mass used to generate quasielastic interactions with its 1σ error is $M_A^{\mathrm{QE}} = 1.21 \pm 0.18$ GeV/c^2, while the Fermi momentum in oxygen is 209 ± 31 MeV/c. Parameters describing contributions from 2p2h interactions, resonant pion production, and deep inelastic scattering follow the assignments in the previous analysis [4]. These parameters' uncertainties induce a ±0.1% uncertainty on the neutron detection efficiency.

Additionally, nucleon FSI uncertainties could cause variations in the number and energy spectrum of neutrons coming from the ν-^{16}O interaction, thereby affecting the neutron detection efficiency. We vary the scattering and particle production probability of the *hA* model [102] within GENIE [103] to assess the possible impact. Assigning a 20% uncertainty to the total rescattering probability, 50% to the charge exchange probability, 30% to the elastic scattering probability, 40% to the inelastic scattering probability, 20% to the absorption probability, and 20% to the pion production probability results in an uncertainty of ±0.4% on the neutron detection efficiency.

5. μ and π capture on ^{16}O

A small portion of CC interactions may generate muons that can be captured by oxygen atoms and consequently produce additional neutrons. Likewise, some neutral current interactions can create pions, whose capture may also produce neutrons. We evaluate the uncertainty from these processes by switching from the intranuclear cascade model to CHIPS [104] within SKDETSIM. The resulting uncertainties on the neutron detection efficiency are: $^{+0.0\%}_{-1.5\%}$ for π^- capture on ^{16}O and $^{+0.0\%}_{-0.5\%}$ for μ^- capture.

Appendix B: Application to Astrophysical Anti-neutrino Searches

The T2K NCQE sample presented in this work is a unique, high-purity sample of NCQE-like events with all of the same kinematic features as the atmospheric NCQE background to DSNB searches in water Cherenkov detectors. It therefore represents a valuable tool for assessing systematic uncertainties in those searches. In the following we discuss features of T2K that will support DSNB searches conducted at SK.

1. Neutron detection algorithm used in the SK DSNB search

Various neutron detection algorithms are available at SK. Focusing on the neutron detection algorithm used in the DSNB search at SK (termed $\mathrm{n_{DSNB}}$ below) [105] we evaluate its performance with the neutron detection algorithm employed in this study (termed $\mathrm{n_{T2K}}$).

The two algorithms diverge in how they handle the neutron candidate vertex, which is a key factor in the time-of-flight (ToF) calculation for neutron candidate features. As most neutrons stay close to the neutrino interaction vertex, $\mathrm{n_{DSNB}}$ adopts the prompt event vertex for the ToF correction. This approach facilitates the search for hydrogen-capture neutrons, $\mathrm{H}(n,\gamma)$, whose vertex is challenging to reconstruct directly due to the low number of PMT hits. However, as the neutron travels farther, the prompt event vertex becomes less accurate for ToF corrections, which results in the neutron detection efficiency depending upon the neutron kinematics.

On the other hand, $\mathrm{n_{T2K}}$ adopts the reconstructed neutron candidate vertex as the vertex for the ToF correction, making it independent of the neutron kinematics. Fig. 16 shows the neutron detection efficiency as a function of the neutron travel distance for both algorithms and confirms the kinematic independence of $\mathrm{n_{T2K}}$. Since SI modeling can affect predicted neutron kinematics, maintaining kinematic independence helps constrain systematic uncertainties associated with SI models in this study.

Table IX compares the performance of $\mathrm{n_{T2K}}$ and $\mathrm{n_{DSNB}}$. Compared to $\mathrm{n_{T2K}}$, $\mathrm{n_{DSNB}}$ achieves a 7.8% higher neutron detection efficiency, though it incurs slightly larger systematic uncertainties due to its depen-

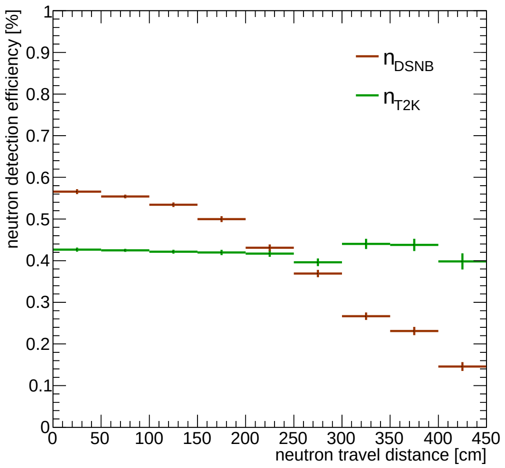

FIG. 16. Neutron detection efficiency versus neutron travel distance for n_{T2K} and n_{DSNB}, with statistical error bars. In n_{DSNB}, the prompt event vertex is used for ToF corrections, making the efficiency more dependent on neutron kinematics. By contrast, n_{T2K} employs the neutron candidate's own vertex for ToF corrections and thus remains relatively independent of the neutron travel distance.

dence on neutron kinematics. Both algorithms perform similarly in terms of purity and η_{Noise}. In order to remain consistent with the DSNB search at SK, the following sections employ n_{DSNB} for further analysis.

TABLE IX. Summary of n_{T2K} and n_{DSNB} for neutron detection efficiency, SI uncertainty, accidental noise rate, and purity. n_{DSNB} offers higher detection efficiency, particularly for H(n,γ), while the n_{DSNB} is less dependent on neutron kinematics and, thus, better at controlling systematic uncertainties.

	n_{T2K}		n_{DSNB}	
	H(n,γ)	Gd(n,γ)	H(n,γ)	Gd(n,γ)
neutron detection efficiency	3.1%	40.0%	8.4%	42.5%
	Overall		Overall	
neutron detection efficiency (ϵ_n)	43.1%		50.9%	
SI model syst. on ϵ_n	$+0.0\%/-0.8\%$		$+1.7\%/-3.4\%$	
Acc. noise rate (η_{Noise})	1.28%		1.47%	
Purity	98.7%		98.3%	

2. Prompt events features with neutron detection

The reconstructed energy and Cherenkov angle distributions of T2K NCQE-like events have been studied in detail previously [4]. However, this is the first time that neutron detection has been applied to T2K NCQE-like events. Since the DSNB signal includes a neutron in the final state, the present sample is unique for examining the kinematic features of NCQE-like events accompanied by neutrons.

The top plots in Fig. 17 compare the reconstructed energy and Cherenkov angle of the T2K NCQE-like sample across different neutron capture multiplicities. The blue dashed line represents prompt events with zero detected neutrons, the red line corresponds to those with one neutron, and the orange dashed line depicts those with more than one neutron. For events with zero neutrons, the reconstructed energy is generally lower, and the Cherenkov angle distribution has a taller peak around 42°, which is consistent with light from a single γ. Conversely, events with multiple detected neutrons tend to have higher reconstructed energies, leading to a concentration of multiple γ events near 90° in the Cherenkov angle distribution.

The bottom six plots of Fig. 17 display the dataset alongside MC predictions, with results organized by neutron capture multiplicity. The second row corresponds to zero neutrons, the third row represents one neutron, and the bottom row illustrates cases with more than one neutron. Notably, the bottom right panel of Fig. 17 illustrates the Cherenkov angle distribution for events with more than one detected neutron. It is observed that the majority of data points cluster around approximately 42° in the Cherenkov angle distribution, whereas MC predictions indicate that most events should concentrate around 90°. This discrepancy may be attributed to the limited statistics in this study. In the near future, the statistical sample could be enhanced by the data set collected during the pure water phase, corresponding to 14.94×10^{20} POT, which is about 8.5 times the neutrino beam exposure used in this study. The statistics could also be improved by utilizing future data sets with a ~0.03% Gd concentration at SK [91].

3. Multiple scattering goodness

The multiple scattering goodness (*MSG*) is a reconstructed parameter recently introduced in the DSNB analysis flow at SK [105], though it was originally developed for the solar neutrino analysis [106]. This parameter is designed to assess the extent to which a particle has scattered during propagation in the detector by analyzing the pattern of PMT hits to determine their anisotropy. At energies relevant to this analysis and the DSNB study at SK, lower energy electrons are more likely to undergo multiple Coulomb scattering than those at higher energies. As a result, the lower energy particles typically produce a more isotropic pattern of hits after multiple scatterings. Since events with one or multiple γ's have an even more isotropic pattern, *MSG* is useful for separating the single-positron prompt event characteristic of the DSNB signal from NCQE backgrounds. An *MSG* value around 0.5 indicates consistency with a single particle direction, suggesting a more coherent Cherenkov pattern. Lower values indicate more isotropy. The calculation of the *MSG* is detailed in Ref. [106].

The *MSG* distribution of T2K NCQE-like events in Run 11, as shown in the left plot of Fig. 18. The histogram is generated using SKG4 with the BERT SI model, while the red dotted and black dashed lines correspond to the SI models INCL++ and BIC, respectively. The right plot of Fig. 18 displays the θ_C versus *MSG* distribution, where delayed signal multiplicities are labeled as follows: zero neutrons are marked with blue squares, one neutron with red circles, and more than one neutron with orange triangles. We note that the NCQE-like events tend to populate lower *MSG* values as expected. The distribution itself is a valuable tool for estimating uncertainties in the DSNB analysis stemming from this paramater.

The *MSG* distribution varies with energy as is shown in Fig. 19 (3.49 to 7.49 MeV) and Fig. 20 (7.49 to 29.49 MeV). The agreement between the data and MC in both figures supports the use of *MSG* information to exclude NCQE events in the DSNB study. Fig. 20 is particularly significant as it focuses on the reconstructed energy range that overlaps with the DSNB search. The efficiency of a $MSG > 0.38$ cut, shown in the left plot of Fig. 20, is 21.4% ± 17.1% (stat.). In the right plot, the gray region highlights the naive cut settings for the DSNB search region at SK, defined as $38^\circ < \theta_\mathrm{C} < 53^\circ$ with $MSG > 0.37$. However, we note that the cuts used in the SK DSNB search [105] will be determined on an energy bin-by-bin basis. The information presented here will be useful for a more detailed assessment of the systematic uncertainties associated with the *MSG* selection applied between atmospheric NCQE and DSNB events.

[1] K. Abe *et al.* (Super-Kamiokande Collaboration), Diffuse supernova neutrino background search at Super-Kamiokande, Phys. Rev. D **104**, 122002 (2021), arXiv:2109.11174 [astro-ph.HE].

[2] M. Harada *et al.* (Super-Kamiokande Collaboration), Search for Astrophysical Electron Antineutrinos in Super-Kamiokande with 0.01% Gadolinium-loaded Water, Astrophys. J. Lett. **951**, L27 (2023), arXiv:2305.05135 [astro-ph.HE].

[3] A. M. Ankowski, O. Benhar, T. Mori, R. Yamaguchi, and M. Sakuda, Analysis of γ-ray production in neutral-current neutrino-oxygen interactions at energies above 200 MeV, Phys. Rev. Lett. **108**, 052505 (2012), arXiv:1110.0679 [nucl-th].

[4] K. Abe *et al.* (The T2K Collaboration), Measurement of neutrino and antineutrino neutral-current quasielasticlike interactions on oxygen by detecting nuclear deexcitation γ rays, Phys. Rev. D **100**, 112009 (2019), arXiv:1910.09439 [hep-ex].

[5] L. Wan *et al.* (Super-Kamiokande Collaboration), Measurement of the neutrino-oxygen neutral-current quasielastic cross section using atmospheric neutrinos at Super-Kamiokande, Phys. Rev. D **99**, 032005 (2019), arXiv:1901.05281 [hep-ex].

[6] S. Sakai *et al.* (Super-Kamiokande Collaboration), Measurement of the neutrino-oxygen neutral-current quasielastic cross section using atmospheric neutrinos in the SK-Gd experiment, Phys. Rev. D **109**, L011101 (2024), arXiv:2311.03842 [hep-ex].

[7] K. Abe *et al.* (The T2K Collaboration), The T2K Experiment, Nucl. Instrum. Meth. A **659**, 106 (2011), arXiv:1106.1238 [physics.ins-det].

[8] K. Abe *et al.* (The T2K Collaboration), T2K neutrino flux prediction, Phys. Rev. D **87**, 012001 (2013), [Addendum: Phys.Rev.D 87, 019902 (2013)], arXiv:1211.0469 [hep-ex].

[9] T. Sekiguchi *et al.* (The T2K Collaboration), Development and operational experience of magnetic horn system for T2K experiment, Nucl. Instrum. Meth. A **789**, 57 (2015), arXiv:1502.01737 [physics.ins-det].

[10] K. Suzuki *et al.* (The T2K Collaboration), Measurement of the muon beam direction and muon flux for the T2K neutrino experiment, PTEP **2015**, 053C01 (2015), arXiv:1412.0194 [physics.ins-det].

[11] M. Antonova *et al.* (Baby MIND), Baby MIND: A Magnetized Segmented Neutrino Detector for the WAGASCI Experiment, JINST **12** (07), C07028, arXiv:1705.10406 [physics.ins-det].

[12] K. Abe *et al.* (The T2K Collaboration), Measurements of the T2K neutrino beam properties using the INGRID on-axis near detector, Nucl. Instrum. Meth. A **694**, 211 (2012), arXiv:1111.3119 [physics.ins-det].

[13] P. A. Amaudruz *et al.* (T2K ND280 FGD Collaboration), The T2K Fine-Grained Detectors, Nucl. Instrum. Meth. A **696**, 1 (2012), arXiv:1204.3666 [physics.ins-det].

[14] N. Abgrall *et al.* (T2K ND280 TPC Collaboration), Time Projection Chambers for the T2K Near Detectors, Nucl. Instrum. Meth. A **637**, 25 (2011), arXiv:1012.0865 [physics.ins-det].

[15] Y. Fukuda *et al.* (Super-Kamiokande Collaboration), The Super-Kamiokande detector, Nucl. Instrum. Meth. A **501**, 418 (2003).

[16] K. Abe *et al.* (Super-Kamiokande Collaboration), First gadolinium loading to Super-Kamiokande, Nucl. Instrum. Meth. A **1027**, 166248 (2022), arXiv:2109.00360 [physics.ins-det].

[17] G. Battistoni, S. Muraro, P. R. Sala, F. Cerutti, A. Ferrari, S. Roesler, A. Fasso, and J. Ranft, The FLUKA code: Description and benchmarking, AIP Conf. Proc. **896**, 31 (2007).

[18] R. Brun, F. Bruyant, F. Carminati, S. Giani, M. Maire, A. McPherson, G. Patrick, and L. Urban, *GEANT Detector Description and Simulation Tool* (1994).

[19] N. Abgrall *et al.* (NA61/SHINE Collaboration), Measurements of $\pi^{\pm}$, $\mathrm{K}^{\pm}$ and proton double differential yields from the surface of the T2K replica target for incoming 31 GeV/c protons with the NA61/SHINE spectrometer at the CERN SPS, Eur. Phys. J. C **79**, 100 (2019), arXiv:1808.04927 [hep-ex].

[20] N. Abgrall *et al.* (NA61/SHINE Collaboration), Measurements of Cross Sections and Charged Pion Spectra in Proton-Carbon Interactions at 31 GeV/c, Phys. Rev. C **84**, 034604 (2011), arXiv:1102.0983 [hep-ex].

[21] N. Abgrall *et al.* (NA61/SHINE Collaboration), Measurement of Production Properties of Positively Charged Kaons in Proton-Carbon Interactions at 31 GeV/c, Phys. Rev. C **85**, 035210 (2012),

arXiv:1112.0150 [hep-ex].

[22] N. Abgrall *et al.* (NA61/SHINE Collaboration), Measurements of $\pi^{\pm}$, $\mathrm{K}^{\pm}$, K^0_S , Λ and proton production in proton–carbon interactions at 31 GeV/c with the NA61/SHINE spectrometer at the CERN SPS, Eur. Phys. J. C **76**, 84 (2016), arXiv:1510.02703 [hep-ex].

[23] K. Abe *et al.* (T2K), Measurements of neutrino oscillation parameters from the T2K experiment using 3.6×10^{21} protons on target, Eur. Phys. J. C **83**, 782 (2023), arXiv:2303.03222 [hep-ex].

[24] C. Zeitnitz and T. A. Gabriel, The GEANT - CALOR interface and benchmark calculations of ZEUS test calorimeters, Nucl. Instrum. Meth. A **349**, 106 (1994).

[25] S. Agostinelli *et al.* (GEANT4), GEANT4 - A Simulation Toolkit, Nucl. Instrum. Meth. A **506**, 250 (2003).

[26] S. Sakai, Measurement of the neutrino-oxygen neutral-current quasielastic cross section and study of nucleon-nucleus interaction model using atmospheric neutrino data in the SK-Gd experiment, Ph.D. thesis, Okayama University (2024).

[27] Y. Hayato and L. Pickering, The NEUT neutrino interaction simulation program library, Eur. Phys. J. ST **230**, 4469 (2021), arXiv:2106.15809 [hep-ph].

[28] Y. Hayato, A neutrino interaction simulation program library NEUT, Acta Phys. Polon. B **40**, 2477 (2009).

[29] H. W. Bertini, Nonelastic Interactions of Nucleons and π Mesons with Complex Nuclei at Energies Below 3 Gev, Phys. Rev. C **6**, 631 (1972).

[30] R. D. Woods and D. S. Saxon, Diffuse Surface Optical Model for Nucleon-Nuclei Scattering, Phys. Rev. **95**, 577 (1954).

[31] O. Benhar, N. Farina, H. Nakamura, M. Sakuda, and R. Seki, Electron- and neutrino-nucleus scattering in the impulse approximation regime, Phys. Rev. D **72**, 053005 (2005), arXiv:hep-ph/0506116.

[32] S. Abe, Implementation and investigation of electron-nucleus scattering in the neut neutrino event generator, Phys. Rev. D **111**, 033006 (2025), arXiv:2412.07466 [hep-ph].

[33] R. Bradford, A. Bodek, H. Budd, and J. Arrington, A New Parameterization of the Nucleon Elastic Form Factors, Nucl. Phys. B Proc. Suppl. **159**, 127 (2006).

[34] J. Nieves, I. Ruiz Simo, and M. J. Vicente Vacas, Inclusive Charged–Current Neutrino–Nucleus Reactions, Phys. Rev. C **83**, 045501 (2011), arXiv:1102.2777 [hep-ph].

[35] D. Rein and L. M. Sehgal, Neutrino Excitation of Baryon Resonances and Single Pion Production, Annals Phys. **133**, 79 (1981).

[36] C. Berger and L. M. Sehgal, Lepton mass effects in single pion production by neutrinos, Phys. Rev. D **76**, 113004 (2007), arXiv:0709.4378 [hep-ph].

[37] K. M. Graczyk and J. T. Sobczyk, Lepton mass effects in weak charged current single pion production, Phys. Rev. D **77**, 053003 (2008), arXiv:0709.4634 [hep-ph].

[38] M. Glück, E. Reya, and A. Vogt, Dynamical parton distributions revisited, Eur. Phys. J. C **5**, 461 (1998), arXiv:hep-ph/9806404.

[39] A. Bodek and U. K. Yang, Modeling neutrino and electron scattering inelastic cross-sections in the few GeV region with effective LO PDFs TV Leading Order, in AIP Conf.Proc. 670, 1, 110-117 (2003) arXiv:hep-ex/0308007.

[40] K. Kobayashi *et al.*, De-excitation gamma-rays from the s-hole state in N-15 associated with proton decay in O-16, Preprint (2006), arXiv:nucl-ex/0604006.

[41] M. Leuschner *et al.*, Quasielastic proton knockout from O-16, Phys. Rev. C **49**, 955 (1994).

[42] F. Ajzenberg-Selove, Energy levels of light nuclei A = 13-15, Nucl. Phys. A **523**, 1 (1991).

[43] R. Brun, F. Bruyant, M. Maire, A. McPherson, and P. Zanarini, GEANT 3 : user's guide Geant 3.10, Geant 3.11 (1994).

[44] M. Harada, Geant4 based Simulation Study for Super-Kamiokande, J. Phys. Conf. Ser. **1468**, 012255 (2020).

[45] K. Abe *et al.*, Calibration of the Super-Kamiokande Detector, Nucl. Instrum. Meth. A **737**, 253 (2014), arXiv:1307.0162 [physics.ins-det].

[46] J. O. Johnson and T. A. Gabriel, A user's guide to MICAP: A Monte Carlo Ionization Chamber Analysis Package, ORNL/TM-10340 (1988).

[47] R. Kinsey, Data Formats and Procedures for the Evaluated Nuclear Data File, ENDF/B-V, ENDF-102 (1979).

[48] W. A. Coleman and T. W. Armstrong, THE NUCLEON - MESON TRANSPORT CODE NMTC, ORNL-4606 (1970).

[49] T. W. Armstrong, R. G. Alsmiller, Jr., and B. L. Bishop, Monte carlo calculations of high-energy nucleon-meson cascades and comparison with experiment, Nucl. Sci. Eng. **49**, 82 (1972).

[50] D. H. Wright and M. H. Kelsey, The Geant4 Bertini Cascade, Nucl. Instrum. Meth. A **804**, 175 (2015).

[51] A. Boudard, J. Cugnon, J.-C. David, S. Leray, and D. Mancusi, New potentialities of the Liège intranuclear cascade model for reactions induced by nucleons and light charged particles, Phys. Rev. C **87**, 014606 (2013), arXiv:1210.3498 [nucl-th].

[52] G. Folger, I. V.N., and J. Wellisch, The Binary Cascade, Eur. Phys. J. A **21**, 407 (2004).

[53] J. M. Quesada *et al.*, Recent Developments in Pre-Equilibrium and De-Excitation Models in Geant4, Prog. Nucl. Sci. Technol. **2**, 936 (2011).

[54] J. Meija, T. B. Coplen, M. Berglund, W. A. Brand, P. D. Bièvre, M. Gröning, N. E. Holden, J. Irrgeher, R. D. Loss, T. Walczyk, and T. Prohaska, Isotopic compositions of the elements 2013 (iupac technical report), Pure and Applied Chemistry **88**, 293 (2016).

[55] M. B. Chadwick *et al.*, ENDF/B-VII.1 Nuclear Data for Science and Technology: Cross Sections, Covariances, Fission Product Yields and Decay Data, Nucl. Data Sheets **112**, 2887 (2011).

[56] K. Hagiwara *et al.*, Gamma Ray Spectrum from Thermal Neutron Capture on Gadolinium-157, PTEP **2019**, 023D01 (2019), arXiv:1809.02664 [nucl-ex].

[57] M. Smy (Super Kamiokande Collaboration), Low Energy Event Reconstruction and Selection in Super-Kamiokande-III, in *30th International Cosmic Ray Conference*, Vol. 5 (2007) pp. 1279–1282.

[58] S. Han *et al.* (Super-Kamiokande), Measurement of neutron production in atmospheric neutrino interactions at Super-Kamiokande, Phys. Rev. D **112**, 012004 (2025), arXiv:2505.04409 [hep-ex].

[59] Y. Hino, K. Abe, R. Asaka, S. Han, M. Harada, M. Ishitsuka, H. Ito, S. Izumiyama, Y. Kanemura, Y. Koshio, F. Nakanishi, H. Sekiya, and T. Yano, Modification on Thermal Motion in Geant4 for Neutron Capture Simulation in Gadolinium Loaded Water, PTEP **2025**, 013C01 (2024).

[60] W. Y. Ma, E. S. Pinzon Guerra, M. Yu, A. Fiorentini, and T. Feusels (The T2K Collaboration), Current status of final-state interaction models and their impact on neutrino-nucleus interactions, J. Phys. Conf. Ser. **888**, 012171 (2017).

[61] T. Golan, C. Juszczak, and J. T. Sobczyk, Final State Interactions Effects in Neutrino-Nucleus Interactions, Phys. Rev. C **86**, 015505 (2012), arXiv:1202.4197 [nucl-th].

[62] A. Bodek, H. S. Budd, and M. E. Christy, Neutrino Quasielastic Scattering on Nuclear Targets: Parametrizing Transverse Enhancement (Meson Exchange Currents), Eur. Phys. J. C **71**, 1726 (2011), arXiv:1106.0340 [hep-ph].

[63] S. Abe, Nuclear deexcitation simulator for neutrino interactions and nucleon decays of ^{12}C and ^{16}O based on TALYS, Phys. Rev. D **109**, 036009 (2024), arXiv:2310.10394 [hep-ph].

[64] J. Chakrani *et al.*, Parametrized uncertainties in the spectral function model of neutrino charged-current quasielastic interactions for oscillation analyses, Phys. Rev. D **109**, 072006 (2024), arXiv:2308.01838 [hep-ex].

[65] S. Abe *et al.* (KamLAND Collaboration), First measurement of the strange axial coupling constant using neutral-current quasielastic interactions of atmospheric neutrinos at KamLAND, Phys. Rev. D **107**, 072006 (2023), arXiv:2211.13911 [hep-ex].

[66] L. A. Ahrens *et al.*, Measurement of Neutrino - Proton and anti-neutrino - Proton Elastic Scattering, Phys. Rev. D **35**, 785 (1987).

[67] A. A. Aguilar-Arevalo *et al.* (MiniBooNE Collaboration), Measurement of the Neutrino Neutral-Current Elastic Differential Cross Section on Mineral Oil at $E_\nu \sim$ 1 GeV, Phys. Rev. D **82**, 092005 (2010), arXiv:1007.4730 [hep-ex].

[68] J. Ashman *et al.* (European Muon), An Investigation of the Spin Structure of the Proton in Deep Inelastic Scattering of Polarized Muons on Polarized Protons, Nucl. Phys. B **328**, 1 (1989).

[69] W. M. Alberico, S. M. Bilenky, and C. Maieron, Strangeness in the nucleon: Neutrino - nucleon and polarized electron - nucleon scattering, Phys. Rept. **358**, 227 (2002), arXiv:hep-ph/0102269.

[70] A. Airapetian *et al.* (HERMES Collaboration), Precise determination of the spin structure function g(1) of the proton, deuteron and neutron, Phys. Rev. D **75**, 012007 (2007), arXiv:hep-ex/0609039.

[71] V. Y. Alexakhin *et al.* (COMPASS Collaboration), The Deuteron Spin-dependent Structure Function g1(d) and its First Moment, Phys. Lett. B **647**, 8 (2007), arXiv:hep-ex/0609038.

[72] O. Benhar and D. Meloni, Total neutrino and antineutrino nuclear cross-sections around 1-GeV, Nucl. Phys. A **789**, 379 (2007), arXiv:hep-ph/0610403.

[73] S. Abe (KamLAND Collaboration), Nuclear deexcitation associated with neutrino-carbon interactions, J. Phys. Conf. Ser. **2156**, 012189 (2021).

[74] A. Koning, S. Hilaire, and S. Goriely, TALYS: modeling of nuclear reactions, Eur. Phys. J. A **59**, 146 (2023).

[75] W. Hauser and H. Feshbach, The Inelastic Scattering of Neutrons, Phys. Rev. **87**, 366 (1952).

[76] R. Akutsu, A Study of Neutrons Associated with Neutrino and Antineutrino Interactions on the Water Target at the T2K Far Detector, Ph.D. thesis, University of Tokyo (2019).

[77] M. T. Nieslony, *Towards a neutron multiplicity measurement with the Accelerator Neutrino Neutron Interaction Experiment*, Ph.D. thesis, Mainz U. (2022).

[78] M. Elkins *et al.* (MINERvA Collaboration), Neutron measurements from antineutrino hydrocarbon reactions, Phys. Rev. D **100**, 052002 (2019), arXiv:1901.04892 [hep-ex].

[79] B. Aharmim *et al.* (SNO Collaboration), Measurement of Neutron Production in Atmospheric Neutrino Interactions at the Sudbury Neutrino Observatory, Phys. Rev. D **99**, 112007 (2019), arXiv:1904.01148 [hep-ex].

[80] V. F. Weisskopf and D. H. Ewing, On the Yield of Nuclear Reactions with Heavy Elements, Phys. Rev. **57**, 472 (1940).

[81] S. Furihata, K. Niita, S. Meigo, Y. Ikeda, and F. Maekawa, The GEM Code- A Simulation Program for the Evaporation and Fission Process of an Excited Nucleus, JAERI-Data/Code 2001-015 , Japan Atomic Energy Research Institute (JAERI) (2001).

[82] K. Abe *et al.* (Hyper-Kamiokande Proto-Collaboration), Hyper-Kamiokande Design Report, Preprint (2018), arXiv:1805.04163 [physics.ins-det].

[83] F. An *et al.* (JUNO Collaboration), Neutrino Physics with JUNO, J. Phys. G **43**, 030401 (2016), arXiv:1507.05613 [physics.ins-det].

[84] P. deNiverville, D. McKeen, and A. Ritz, Signatures of sub-GeV dark matter beams at neutrino experiments, Phys. Rev. D **86**, 035022 (2012), arXiv:1205.3499 [hep-ph].

[85] P. deNiverville, C.-Y. Chen, M. Pospelov, and A. Ritz, Light dark matter in neutrino beams: production modelling and scattering signatures at MiniBooNE, T2K and SHiP, Phys. Rev. D **95**, 035006 (2017), arXiv:1609.01770 [hep-ph].

[86] P. Adamson *et al.* (MINOS Collaboration), Active to sterile neutrino mixing limits from neutral-current interactions in MINOS, Phys. Rev. Lett. **107**, 011802 (2011), arXiv:1104.3922 [hep-ex].

[87] P. Adamson *et al.* (NOvA Collaboration), Search for active-sterile neutrino mixing using neutral-current interactions in NOvA, Phys. Rev. D **96**, 072006 (2017), arXiv:1706.04592 [hep-ex].

[88] K. Abe *et al.* (The T2K Collaboration), Search for light sterile neutrinos with the T2K far detector Super-Kamiokande at a baseline of 295 km, Phys. Rev. D **99**, 071103 (2019), arXiv:1902.06529 [hep-ex].

[89] K. Abe *et al.* (The T2K Collaboration), Proposal for an Extended Run of T2K to 20 × 10^{21} POT, Preprint (2016), arXiv:1609.04111 [hep-ex].

[90] H. Watanabe *et al.* (Super-Kamiokande Collaboration), First Study of Neutron Tagging with a Water Cherenkov Detector, Astropart. Phys. **31**, 320 (2009), arXiv:0811.0735 [hep-ex].

[91] K. Abe *et al.* (Super-Kamiokande Collaboration), Second gadolinium loading to Super-Kamiokande, Nucl. Instrum. Meth. A **1065**, 169480 (2024), arXiv:2403.07796 [physics.ins-det].

[92] Y. Ashida *et al.*, Measurement of γ-ray production via the neutron-^{16}O reaction using a 77 MeV quasimonoenergetic neutron beam, Phys. Rev. C **109**, 014620 (2024), arXiv:1902.08964 [nucl-ex].

[93] T. Tano *et al.*, Measurement of γ-Rays Generated by Neutron Interaction with ^{16}O at 30 MeV and 250 MeV,

PTEP **2024**, 113D01 (2024), arXiv:2405.15366 [nucl-ex].

[94] Y. Hino, Y. Ashida, T. Tano, and Y. Koshio, A simulation model investigation of neutron-oxygen inelastic scattering and subsequent nucleus deexcitation based on experimental data, Preprint (2025), arXiv:2506.14388.

[95] D. Chiesa, C. Cazzaniga, M. Nastasi, M. Rebai, C. D. Frost, G. Gorini, S. Lilley, S. Pozzi, and E. Previtali, Measurements of Neutron Fields in a Wide Energy Range Using Multi-Foil Activation Analysis, IEEE Trans. Nucl. Sci. **69**, 1659 (2022), arXiv:2110.05073 [physics.ins-det].

[96] Y. Shimizu *et al.*, SAMURAI project at RIBF, J. Phys. Conf. Ser. **312**, 052022 (2011).

[97] A. Hiramoto *et al.* (NINJA Collaboration), First measurement of $\overline{\nu}_\mu$ and ν_μ charged-current inclusive interactions on water using a nuclear emulsion detector, Phys. Rev. D **102**, 072006 (2020), arXiv:2008.03895 [hep-ex].

[98] M. Khachatryan *et al.* (CLAS, e4v), Electron-beam energy reconstruction for neutrino oscillation measurements, Nature **599**, 565 (2021).

[99] T2K Collaboration, Data release for “First measurement of neutron capture multiplicity in neutrino-oxygen neutral-current quasi-elastic-like interactions using an accelerator neutrino beam”, 10.5281/zenodo.15577122 (2025).

[100] K. Abe *et al.* (The T2K Collaboration), Search for CP Violation in Neutrino and Antineutrino Oscillations by the T2K Experiment with 2.2×10^{21} Protons on Target, Phys. Rev. Lett. **121**, 171802 (2018), arXiv:1807.07891 [hep-ex].

[101] K. Abe *et al.* (The T2K Collaboration), Measurement of neutrino and antineutrino oscillations by the T2K experiment including a new additional sample of ν_e interactions at the far detector, Phys. Rev. D **96**, 092006 (2017), [Erratum: Phys.Rev.D 98, 019902 (2018)], arXiv:1707.01048 [hep-ex].

[102] C. Andreopoulos, C. Barry, S. Dytman, H. Gallagher, T. Golan, R. Hatcher, G. Perdue, and J. Yarba, The GENIE Neutrino Monte Carlo Generator: Physics and User Manual, FERMILAB-FN-1004-CD (2015), arXiv:1510.05494 [hep-ph].

[103] C. Andreopoulos *et al.*, The GENIE Neutrino Monte Carlo Generator, Nucl. Instrum. Meth. A **614**, 87 (2010), arXiv:0905.2517 [hep-ph].

[104] M. V. Kossov, Chiral-invariant phase space model. I: Masses of hadrons, Eur. Phys. J. A **14**, 265 (2002).

[105] A. Santos, M. Harada, and Y. Kanemura (Super-Kamiokande Collaboration), New limits on the low-energy astrophysical electron antineutrinos at SK-Gd experiment, Neutrino 2024 (Poster) (2024).

[106] K. Abe *et al.* (Super-Kamiokande Collaboration), Solar Neutrino Measurements in Super-Kamiokande-IV, Phys. Rev. D **94**, 052010 (2016), arXiv:1606.07538 [hep-ex].

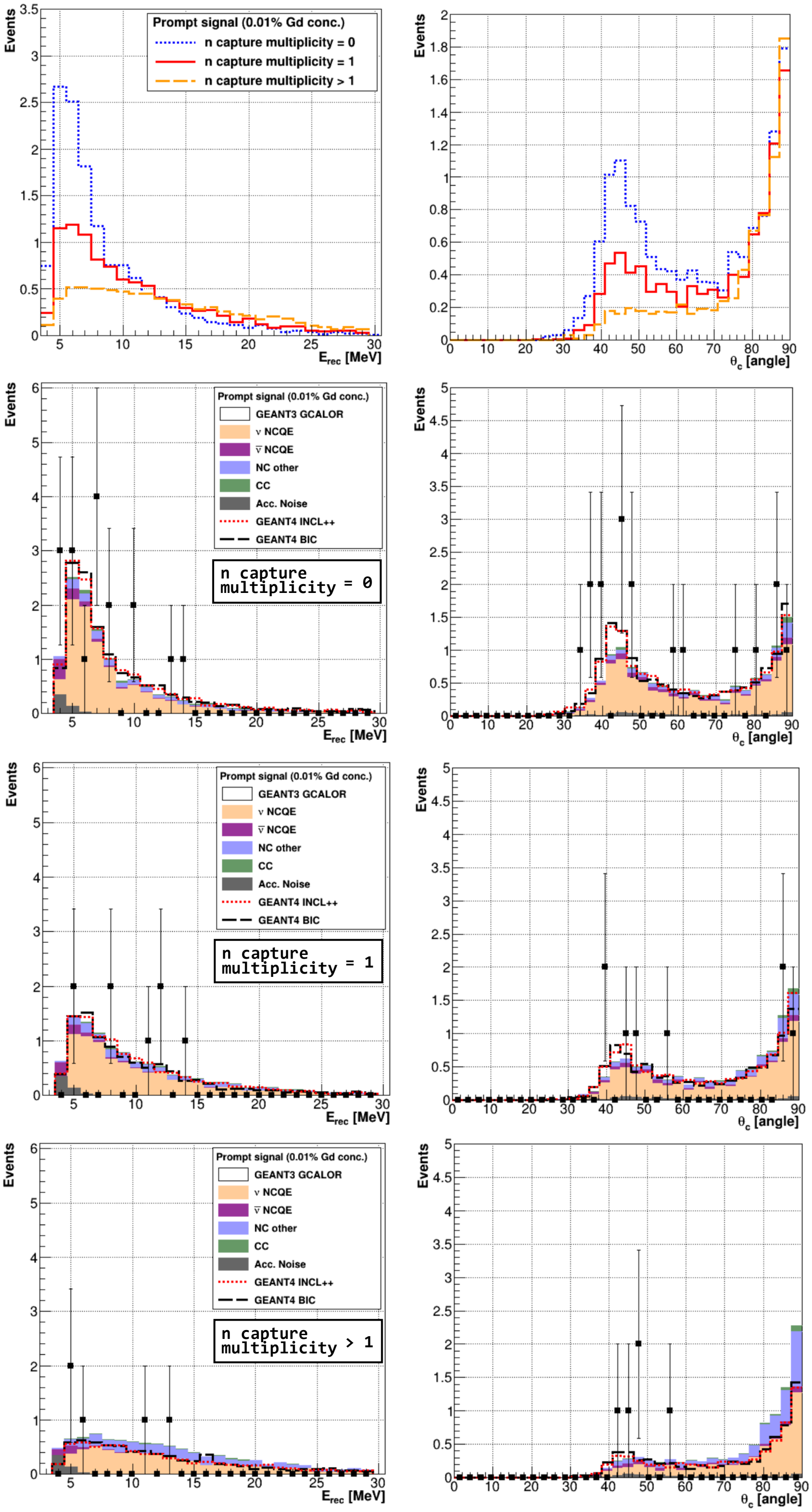

FIG. 17. Reconstructed energy and Cherenkov angle distributions for NCQE-like prompt events are shown, categorized by neutron capture multiplicity (zero: dotted blue, one: solid red, more than one: dashed orange) in the top row. The data set is compared with MC predictions incorporating different SI models, with neutron capture multiplicity information displayed in the second row (zero), the third row (one), and the bottom row (more than one).

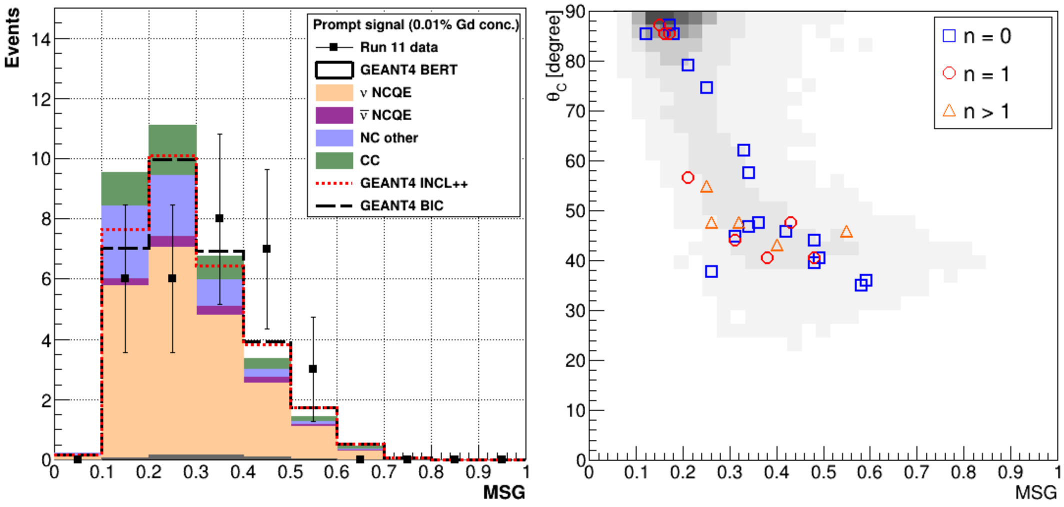

FIG. 18. For both panels, events in the full energy range [3.49, 29.49] MeV are shown. Left panel: *MSG* distributions for prompt events, comparing data set with MC using the BERT SI model (histogram), INCL++ (dotted red), and BIC (dashed black). Right panel: Correlation between Cherenkov angle and *MSG*, with *MSG* ~ 0.5 indicating coherent patterns. Delayed signal multiplicity for each prompt event is categorized as zero (blue squares), one (red circles), or more than one (orange triangles).

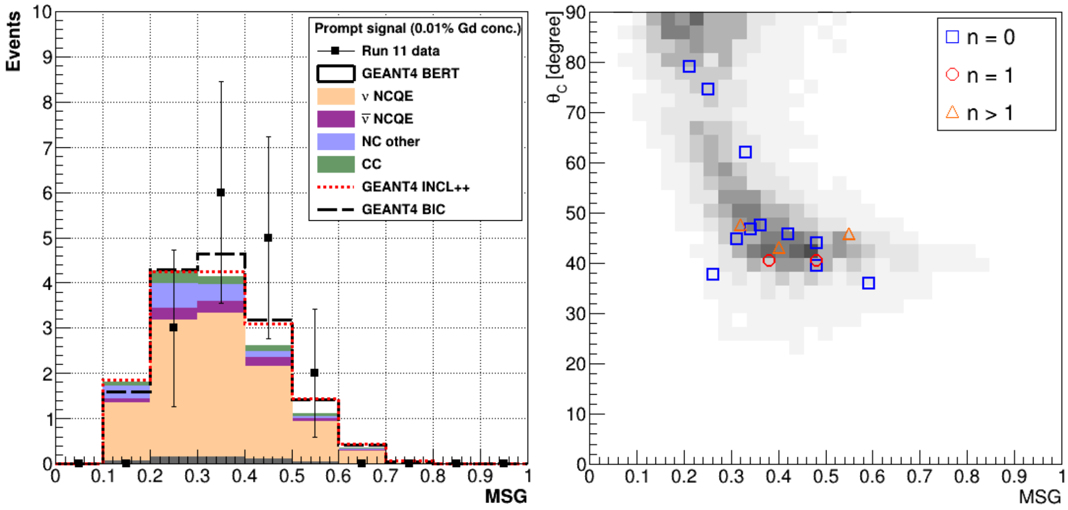

FIG. 19. Comparisons of data and MC predictions for NCQE-like events within the reconstructed energy range of [3.49, 7.49] MeV, showing *MSG* distributions alongside θ_{C}.

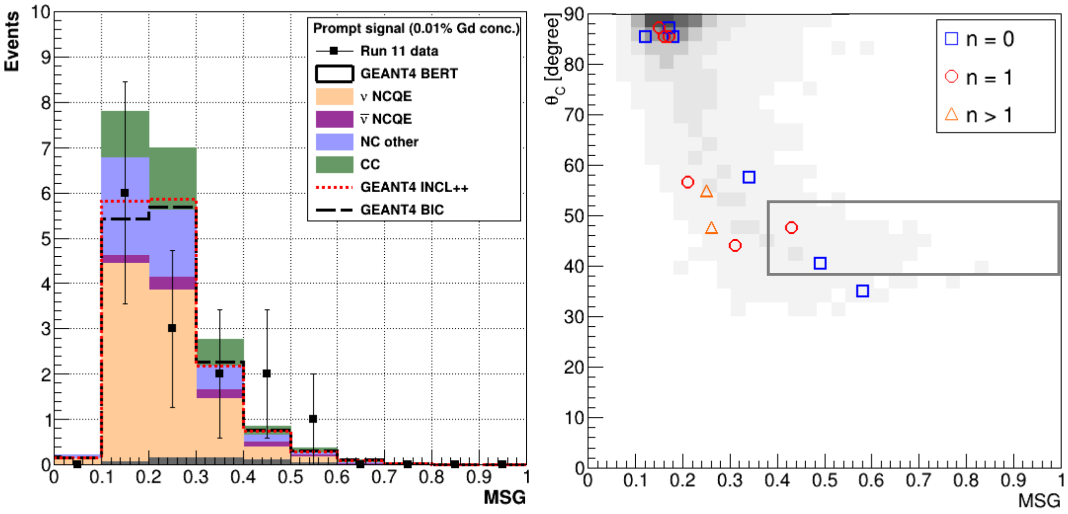

FIG. 20. Same as Fig. 19, but for the higher-energy range of [7.49, 29.49] MeV, which overlaps with the DSNB search window. In the left plot, an *MSG* > 0.38 selection yields an efficiency of 21.4% ± 17.1 (stat.), while the right plot highlights (in gray) the naive DSNB cut region ($38^\circ < \theta_\mathrm{C} < 53^\circ$, *MSG* > 0.37).